Bora, S. S., Cotton, F., Scherbaum, F. (2019): NGA-West2 Empirical Fourier and Duration Models to Generate Adjustable Response Spectra. - *Earthquake Spectra*, *35*, 1, pp. 61—93.

DOI: http://doi.org/10.1193/110317EQS228M

NGA-West2 Empirical Fourier and Duration Models to Generate Adjustable Response Spectra

Sanjay Singh Bora,[a)] Fabrice Cotton,[a),b)] and Frank Scherbaum[b)]

Adjustment of median ground motion prediction equations (GMPEs) from one region to another region is one of the major challenges within the current practice of seismic hazard analysis. In our approach of generating response spectra, we derive two separate empirical models for a) Fourier amplitude spectrum (FAS) and b) duration of ground motion. To calculate response spectra, the two models are combined within the random vibration theory (RVT) framework. The models are calibrated on recordings obtained from shallow crustal earthquakes in active tectonic regions. We use a subset of NGA-West2 database with **M**3.2–7.9 earthquakes at distances 0–300 km. The NGA-West2 database expanded over a wide magnitude and distance range facilitates a better constraint over derived models. A frequency-dependent duration model is derived to obtain adjustable response spectral ordinates. Excellent comparison of our approach with other NGA-West2 models implies that it can also be used as a stand-alone model. [DOI: 10.1193/110317EQS228M]

INTRODUCTION

A reliable estimation of ground motions that can be produced by future earthquakes is an essential element of any seismic hazard analysis study. This is achieved by employing empirically derived ground motion prediction equations (GMPEs) that provide a probabilistic measure of expected ground motion as a function of magnitude, distance, and site condition. Ground motion recordings made from past earthquakes are used to derive such GMPEs. Thus, the GMPEs are often available only for well-monitored active regions such as California (CA) and Japan. However, there are many seismically active regions (e.g., India, Central Europe, and Eastern North America) for which the data are insufficient in the magnitude and distance range of engineering interest, which does not allow for the development of a reliable GMPE for such a region.

To address this problem, several approaches have been suggested. For example, developing a GMPE for a data-poor region using the database that is generated through simulations (Atkinson and Boore 1995, 2006, Toro et al. 1997, Atkinson and Silva 2000, Raghu Kanth and Iyenger 2007, and Rietbrock et al. 2013). Usually, such approaches are based upon stochastic simulations of ground motion (Boore 2003). However, the use of this approach is often limited by the non-availability of well-constrained full sets of stochastic model

[a)] German Research Center for Geosciences, Helmholtzstraße 6, Potsdam 14467, Germany; Email: sanjay.bora@sed.ethz.ch (S. S. B.)
[b)] Institute of Earth and Environmental Science, University of Potsdam, Potsdam, Germany

Earthquake Spectra, Volume 35, No. 1, pages 61–93, February 2019;

parameters for a data-poor region and also by the fact that it does not provide a realistic measure of aleatory variability. Another popular approach is the hybrid empirical method (Campbell 2003). This method adjusts an empirically derived GMPE in the data-rich (host) region for use in the data-poor (target) region, using so-called adjustment factors. The adjustment factors are computed from ratios of stochastically simulated response spectral ordinates in the target and host regions. A third method is the reference-based empirical approach (Atkinson 2008), which also utilizes the adjustment factors but are determined from the response spectral ratios of the observed data in the target and host regions. Recently, Yenier and Atkinson (2015) suggested an approach that is essentially based upon the point-source stochastic simulation of ground motions. In this method, a response spectral GMPE is derived for the host region using the simulated data, which is subsequently adjusted to a target region by plugging in the corresponding target parameter, e.g., the stress parameter.

Recently, it was shown by Stafford et al. (2017) that linear amplification factors computed for response spectra at high oscillator frequencies exhibit scenario dependence, mainly for smaller-magnitude events. This is due to the fact that a response spectrum at high oscillator frequencies captures the strength of the corresponding Fourier spectrum over a broad range of frequencies, as shown in detail by Bora et al. (2016). Moreover, from a signal processing perspective, the adjustment problem of a ground motion model essentially belongs to the realm of linear systems. Keeping in mind this basic concept, Bora et al. (2014, 2015) presented an alternative modeling framework, in which the problem of adjustment is mainly dealt with in the Fourier domain. Essentially, this approach comprises developing two separate empirical models for the Fourier amplitude spectrum (FAS) and duration of ground motion. Thus, in this framework, the necessary adjustments for a selected seismological parameter (e.g., stress parameter or kappa) are made in the Fourier and duration domain. The predicted and/or adjusted FAS and duration are combined within the random vibration theory framework to obtain the corresponding adjusted response spectra. Additionally, the Fourier domain provides a direct way to examine the expected behavior of a particular seismological parameter on the ground motion, while there is no one-to-one correspondence between FAS and response spectrum, particularly at high oscillator frequencies (Bora et al. 2016, Montejo and Vidot-Vega 2017).

This approach was initially implemented (Bora et al. 2014, 2015) on a limited European database (RESORCE-2012; Akkar et al. 2014). In this article, we calibrate our approach on a much larger NGA-West2 database (Ancheta et al. 2014), which is significantly expanded in terms of magnitude, distance, and site condition ranges. Thus, it provides a better constraint over derived model parameters. For our analysis, we consider a subset of the larger parent database, which contains 285 events in the magnitude range **M**3.2–7.9, 11,387 biaxial (total 22,774) acceleration recordings made at 3,446 stations in the distance range of 0–300 km. In the selected dataset, the majority of the recordings are from CA with 63.3%, Taiwan (TW) and Japan with an equal 15.4%, and very few recordings from Italy (IT) at ~2.5%. All the earthquakes considered in this study are shallow crustal events.

The measure of ground motion duration that is used in our approach is unique in the sense that it is not determined directly from the acceleration trace. Given the (observed) FAS of an acceleration trace, we define the duration as having the value that is required for an RVT-computed response spectrum to be matched with the observed response spectrum. In this

process, the optimization is performed at each oscillator frequency of the single degree of freedom (SDOF) oscillator (for details see the section *RVT and Duration Estimation*) for a selected damping ratio (in this case, 5% of critical damping). This allows us to derive an oscillator frequency–dependent duration model. Our empirical models for both FAS and duration are simple and include only moment magnitude (**M**), Rupture distance (R_{rup}), and time-averaged shear-wave velocity in the upper 30 m beneath the station (V_{S30}) as the predictor variables.

Finally, a consistency check is performed by showing comparisons of the median predictions and aleatory variability obtained from our approach with that from recently derived NGA-West2 GMPEs. The agreement of our results with the NGA-West2 GMPEs indicates that this modeling framework can be used as a standalone model as with other NGA-West2 models. However, additional benefits of having two separate models for the FAS and ground motion duration are that they are much easier to adjust to particular target regions than traditional empirical GMPEs.

DATA

We used acceleration time histories and a flat file available from the NGA-West2 database (Ancheta et al. 2014). Although the original database consists of more than 20,000 records, we used a subset of the full database. Many records (mainly from the Wenchuan earthquake and Iranian events) were not available in the online database. In addition to that, we selected events that are assigned **M** and records recorded at a distance of less than $R_{rup} \leq 300$ km. We also discarded recordings, which were made at stations with $V_{S30} \leq 200$ m/s. The final database used for our analysis consists of 11,387 biaxial acceleration recordings made at 3,446 stations from 285 earthquakes in a magnitude range **M**3.2–7.9. The flat file describing the used metadata is available in the online Appendix.

The main metadata features of our selected dataset are summarized in Figure 1. The magnitude and distance (R_{rup}) distributions for different soil types are shown in Figure 1a, 1b, and 1c. For Figure 1, the station sites have been subdivided into different soil types based upon their V_{S30} values: $200 < V_{S30} < 400$ m/s as soft, $400 \leq V_{S30} < 800$ as stiff, and $V_{S30} \geq 800$ m/s as rock (or hard rock). We clearly see that for the soft and stiff soil categories, the data is well sampled in the terms of magnitude and distance distribution. However, recordings at rock sites are very sparse. Figure 1d depicts the number of recordings used in our analysis at each selected frequency separated by the soil types. A significant decrease in the data below 0.3–0.4 Hz can be observed. It is worth mentioning here that the FAS have been smoothed using the Konno and Ohmachi (1998) filter with the default parameter values (i.e., bandwidth = 40). For both the FAS and duration model development, the minimum useable frequency for each record was fixed to be equal to 1.25 times the high-pass-frequency indicated in the flat file. It is also worth mentioning that we use individual component records (i.e., two horizontal components) in our analysis. Mainly because (1) no consistent definition of an average component is available for the FAS and duration of ground motion and (2) an average component underestimates the actual variability in the ground motion.

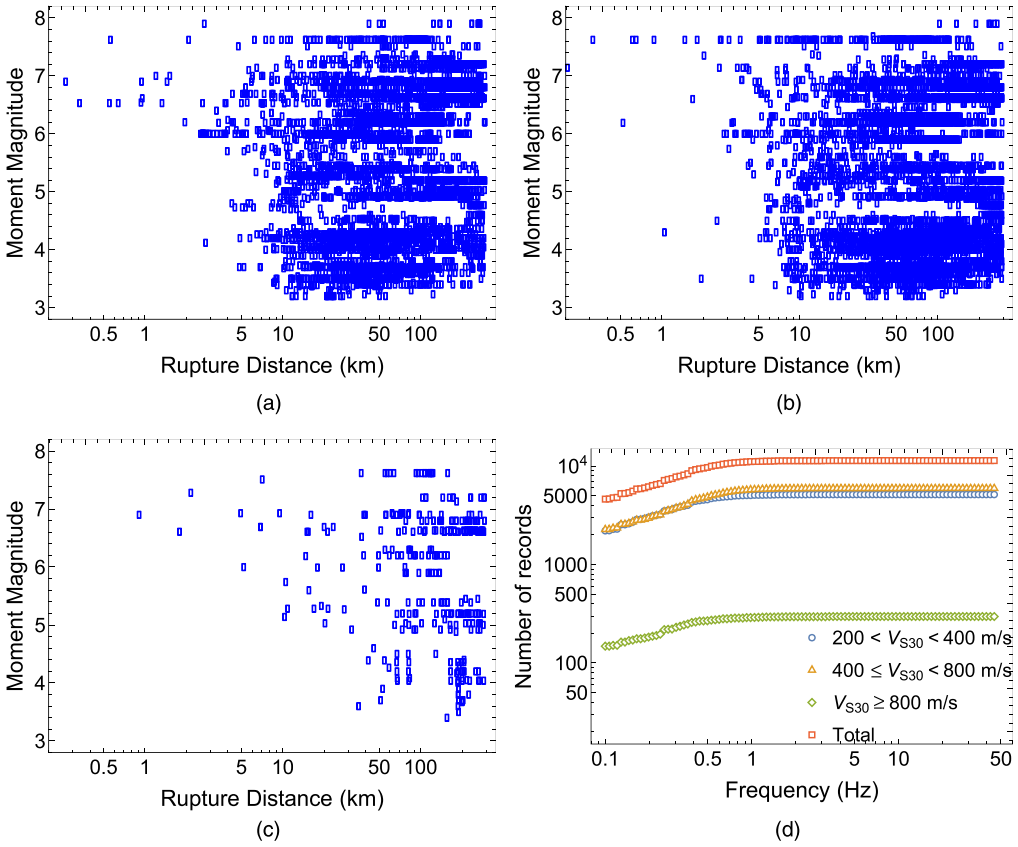

Figure 1. Summary of metadata information. Magnitude-distance distribution of the dataset for (a) $200 < V_{S30} < 400\,\mathrm{m/s}$, (b) $400 \leq V_{S30} < 800\,\mathrm{m/s}$, and (c) $V_{S30} \geq 800\,\mathrm{m/s}$. (d) Number of records available at each selected frequency for station site categories in (a), (b), and (c).

EMPIRICAL FAS MODEL

Analytically, the far field Fourier spectrum of ground motion is often modeled with a Brune (1970, 1971) omega-square source model, which is modified to account for geometrical and anelastic attenuation effects. Boore (2003) has shown a simple yet powerful application of this model in his stochastic simulation technique. An obvious choice would be to use the full stochastic model as the functional form for our FAS model. However, this automatically invites a preferred source model (hence, shape) to be imposed a priori. Also, to keep similarity with the commonly used functional forms for response spectral GMPEs, our attempt was to select a simple, functional form, yet one powerful enough to capture the observed scaling of ground motion with often-used predictor variables, such as magnitude, distance, and V_{S30}. Although recently published NGA-West2 GMPEs (Abrahamson et al. 2014, Boore et al. 2014, Campbell and Bozorgnia 2014, and Chiou and Youngs 2014,

hereafter respectively referred to as ASK14, BSSA14, CB14, and CY14) have suggested complicated functional forms, recently Bindi et al. (2017) used a rather simple functional form to derive their application-specific GMPE from the NGA-West2 database. We also selected a simple, functional form for our FAS model with a lesser number of predictor variables, as follows:

$$\ln Y(f) = c_0 + F_E(\mathbf{M}) + F_P(R_{rup}, \mathbf{M}) + F_S(V_{S30}) + \eta_e + \eta_s + \varepsilon \tag{1}$$

where Y represents the Fourier spectral amplitude (in m/s) at frequency f, and F_E, F_P, and F_S represent functions for source, path, and site effects, respectively. η_e, η_s and ε represent between-event, between-station, and single-station within-event residuals, respectively (Al Atik et al. 2010). The predictor variables are the moment magnitude ($\mathbf{M}$), rupture distance (R_{rup}), and V_{S30} (time-averaged shear-wave velocity in upper 30 m of the soil column).

The source (event) function F_E is given by the following:

$$F_E = \begin{cases} c_1(\mathbf{M} - \mathbf{M}_h) + c_2(8.5 - \mathbf{M})^2 & \mathbf{M} \le \mathbf{M}_h \\ c_3(\mathbf{M} - \mathbf{M}_h) + c_2(8.5 - \mathbf{M})^2 & \mathbf{M} > \mathbf{M}_h \end{cases} \tag{2}$$

Based upon our preliminary regression checks, we selected a frequency-independent value for $M_h = 5$. We also checked the break in magnitude scaling at other magnitudes; the one resulting in least variance was selected.

Our path function F_P is a combination of a standard bilinear geometrical spreading function $G(\mathbf{M}, R_{rup})$ and anelastic attenuation term as follows:

$$F_P = G(\mathbf{M}, R_{rup}) + c_5\left(\sqrt{R_{rup}^2 + h^2} - R_0\right) \tag{3}$$

where the geometrical spreading term G is given by the following equation:

$$G = \begin{cases} [b_1 + c_7(\mathbf{M} - 4.5)] ln \frac{\sqrt{R_{rup}^2 + h^2}}{R_0} & R_{rup} \le R_1 \\ [b_1 + c_7(\mathbf{M} - 4.5)] ln \frac{\sqrt{R_1^2 + h^2}}{R_0} + [b_2 + c_7(\mathbf{M} - 4.5)] ln \frac{\sqrt{R_{rup}^2 + h^2}}{\sqrt{R_1^2 + h^2}} & R_{rup} > R_1 \end{cases} \tag{4}$$

The finite-fault factor term h is chosen to be magnitude dependent as follows:

$$h = \begin{cases} 2 & \mathbf{M} \le 4 \\ c_4 - (c_4 - 1)(5 - \mathbf{M}) & 4 < \mathbf{M} \le 5 \\ c_4 & \mathbf{M} > 5 \end{cases} \tag{5}$$

The reference distance R_0 in Equation 4 was chosen to be 1 km, while the transition distance R_1 was fixed at 50 km. From a set of values, this selection of transition distance offers an appropriate balance between physically expected behavior and the ability of the model to reduce uncertainty.

Since we discarded the station sites with $V_{S30} \le 200$ m/s, and also because it is difficult to capture the nonlinear site effects from the recorded ground motions

(Seyhan and Stewart 2014), we selected a linear site response term in our site function F_S, as follows:

$$F_S = \begin{cases} c_6 \log \frac{V_{S30}}{V_{ref}} & Vs_{30} < V_c \\ c_6 \log \frac{V_c}{V_{ref}} & Vs_{30} \geq V_c \end{cases} \quad (6)$$

where the reference rock velocity $V_{ref} = 800\,\mathrm{m/s}$ and the velocity $V_c = 1{,}100\,\mathrm{m/s}$, beyond which ground motion does not scale with V_{S30}.

The model parameters (i.e., coefficients) of our empirical Fourier model, that is, Equations 1–6, were determined using a random effects regression technique (Bates et al. 2015). This regression technique allows the decomposition of total residuals in between-events and between-station components (η_e and η_s) with zero means and standard deviations τ and ϕ_{S2S}. The standard deviation of the single-station within-event residuals (ε) is represented by ϕ_{SS}. The regression was performed in two iterations; in the first iteration, we limited the data up to 100 km distance, and in the second iteration, the entire dataset is used. In the first iteration, we used a linear geometrical spreading function without the break at 50 km and determined all the coefficients but b_2 and c_5. In the second iteration, c_4 was fixed from the first iteration, and all the remaining coefficients were determined again, including b_1, b_2, and c_5. A frequency-by-frequency regression was performed on smoothed Fourier spectral amplitudes at 100 equally spaced (in log units) frequency points between 0.1–45 Hz. The final coefficients (un-smoothed) and corresponding standard deviations are given in Table 1.

FAS MODEL PREDICTIONS

FAS model predictions are shown in Figure 2. For comparison, FAS model predictions from Bora et al. (2015) are also shown in Figure 2. The distance scaling is shown in Figure 2a and 2b for magnitude $\mathbf{M} = 4.5$ and 7, respectively, at $f = 1.04\,\mathrm{Hz}$. The predictions from the two studies are significantly different, which are primarily due to the differences in the underlying datasets. The differences can also be due to different functional forms adopted in the two studies. For instance, Bora et al. (2015) include a linear geometrical spreading function up to 200 km. It should also be noted that Bora et al. (2015) utilize the Joyner-Boore distance metric, while in the present study rupture distance is used. Magnitude scaling is depicted in Figure 2c at $f = 2.98\,\mathrm{Hz}$ and for the entire spectrum in Figure 2d. The magnitude scaling from this study and that from the study done by Bora et al. (2015) are rather similar for moderate to large magnitudes except the break at **M**5. Full spectral shapes are also similar for the two studies (Figure 2d). The V_{S30} scaling is shown in Figure 2e at $f = 1.04\,\mathrm{Hz}$, while Figure 2f shows the ratio ($V_{S30} = 270\,\mathrm{m/s}$ to $V_{S30} = 800\,\mathrm{m/s}$) of FAS predictions from the two models. Although the absolute values of V_{S30} scaling are different, the scaling (slope) with V_{S30} is similar from both the studies (Figure 2e). The amplification factors shown in Figure 2f also exhibit a difference by a factor of 1.5 between the two curves; however, the shapes are rather similar.

RESIDUALS

The robustness of the selected functional form for the FAS model is evaluated by analyzing residual trends. As an outcome of our mixed-effects regression analysis (Bates et al. 2015) using Equations 1–6, we obtain residuals that are decomposed into event-specific between-event,

Table 1. Coefficients associated with empirical FAS model (Equations 1–6)

f (Hz)	c_0	c_1	c_2	c_3	c_4	c_5	c_6	c_7	b_1	b_2	τ	ϕ_{S2S}	ϕ_{SS}	σ
0.1	2.503	−3.020	−0.699	−0.753	4.696	−0.001	−0.447	0.023	−0.601	−0.617	0.588	0.434	0.619	0.958
0.11	2.493	−2.951	−0.698	−0.702	4.958	−0.001	−0.473	0.008	−0.558	−0.633	0.599	0.449	0.603	0.961
0.11	2.200	−2.752	−0.665	−0.539	5.484	0.000	−0.512	0.001	−0.556	−0.668	0.566	0.466	0.598	0.946
0.12	2.034	−2.516	−0.635	−0.399	5.849	0.000	−0.560	−0.005	−0.581	−0.720	0.590	0.481	0.599	0.969
0.13	1.141	−1.604	−0.533	−0.094	5.480	0.001	−0.602	−0.001	−0.599	−0.808	0.619	0.514	0.595	1.001
0.14	1.098	−1.443	−0.513	0.001	5.656	0.000	−0.649	−0.007	−0.621	−0.807	0.610	0.547	0.580	1.004
0.14	1.483	−1.566	−0.525	−0.040	6.278	0.000	−0.686	−0.015	−0.668	−0.771	0.578	0.572	0.574	0.995
0.15	1.722	−1.532	−0.530	−0.083	7.373	0.000	−0.729	−0.020	−0.687	−0.743	0.568	0.586	0.567	0.994
0.16	1.460	−1.046	−0.487	0.050	8.476	0.000	−0.757	−0.020	−0.722	−0.805	0.567	0.591	0.560	0.993
0.17	1.579	−0.976	−0.483	0.021	9.401	0.000	−0.788	−0.018	−0.735	−0.881	0.559	0.596	0.552	0.986
0.19	1.183	−0.586	−0.438	0.179	9.634	0.000	−0.812	−0.015	−0.732	−0.857	0.551	0.595	0.542	0.976
0.2	1.029	−0.402	−0.419	0.250	9.488	0.000	−0.831	−0.018	−0.723	−0.883	0.549	0.589	0.535	0.967
0.21	1.008	−0.282	−0.403	0.274	9.074	0.000	−0.857	−0.014	−0.749	−0.955	0.538	0.583	0.527	0.952
0.22	0.952	−0.101	−0.381	0.293	8.908	0.000	−0.879	−0.005	−0.779	−0.987	0.537	0.592	0.513	0.950
0.24	1.179	−0.160	−0.390	0.173	8.723	0.000	−0.904	0.002	−0.781	−0.961	0.514	0.603	0.508	0.941
0.25	0.709	0.249	−0.346	0.325	8.630	0.000	−0.913	0.001	−0.755	−0.922	0.494	0.613	0.503	0.934
0.27	1.005	0.122	−0.364	0.231	8.584	−0.001	−0.912	−0.006	−0.735	−0.892	0.482	0.621	0.497	0.930
0.29	1.261	0.032	−0.376	0.152	8.283	−0.001	−0.915	−0.005	−0.745	−0.887	0.467	0.632	0.487	0.924
0.3	1.297	0.092	−0.368	0.124	7.923	−0.001	−0.932	0.001	−0.759	−0.908	0.465	0.637	0.482	0.925
0.32	1.562	−0.060	−0.380	−0.017	7.195	0.000	−0.952	0.012	−0.782	−0.955	0.465	0.645	0.478	0.927
0.34	1.769	−0.211	−0.393	−0.168	6.413	−0.001	−0.976	0.021	−0.769	−0.936	0.476	0.650	0.472	0.934
0.37	1.891	−0.250	−0.397	−0.238	6.522	−0.001	−1.000	0.022	−0.759	−0.834	0.472	0.649	0.469	0.930
0.39	2.131	−0.129	−0.390	−0.134	8.919	−0.001	−1.020	−0.001	−0.828	−0.856	0.459	0.643	0.474	0.922
0.41	2.361	−0.266	−0.398	−0.235	8.864	−0.001	−1.029	0.005	−0.849	−0.893	0.444	0.641	0.466	0.909
0.44	2.526	−0.354	−0.401	−0.319	8.739	−0.001	−1.034	0.016	−0.865	−0.867	0.428	0.642	0.460	0.898
0.47	2.712	−0.425	−0.406	−0.392	9.011	−0.002	−1.045	0.020	−0.868	−0.822	0.408	0.645	0.450	0.886
0.5	2.613	−0.301	−0.389	−0.356	9.331	−0.002	−1.060	0.020	−0.867	−0.804	0.399	0.647	0.444	0.880
0.53	2.320	−0.115	−0.357	−0.283	8.836	−0.002	−1.080	0.029	−0.874	−0.777	0.410	0.647	0.443	0.885
0.56	2.335	−0.049	−0.346	−0.296	8.566	−0.003	−1.079	0.035	−0.883	−0.757	0.414	0.647	0.441	0.886
0.6	2.398	0.036	−0.337	−0.290	8.022	−0.003	−1.065	0.035	−0.897	−0.731	0.420	0.642	0.443	0.886
0.64	2.647	−0.115	−0.351	−0.353	7.624	−0.003	−1.075	0.033	−0.909	−0.702	0.419	0.638	0.441	0.881
0.68	2.848	−0.236	−0.361	−0.424	7.153	−0.004	−1.086	0.034	−0.918	−0.673	0.417	0.636	0.437	0.877
0.72	2.944	−0.324	−0.363	−0.492	6.597	−0.004	−1.073	0.042	−0.916	−0.636	0.409	0.633	0.435	0.871
0.77	2.913	−0.335	−0.356	−0.502	6.467	−0.005	−1.066	0.048	−0.913	−0.597	0.404	0.632	0.435	0.867
0.82	2.835	−0.262	−0.342	−0.480	6.200	−0.005	−1.067	0.050	−0.915	−0.539	0.400	0.632	0.433	0.865
0.87	2.653	−0.090	−0.315	−0.395	6.263	−0.006	−1.063	0.054	−0.934	−0.508	0.408	0.627	0.432	0.864
0.92	2.632	−0.021	−0.302	−0.367	6.867	−0.006	−1.059	0.057	−0.956	−0.501	0.403	0.621	0.431	0.857
0.98	2.616	−0.002	−0.294	−0.367	7.125	−0.006	−1.055	0.061	−0.963	−0.473	0.397	0.618	0.429	0.851
1.04	2.316	0.199	−0.263	−0.268	6.945	−0.007	−1.041	0.067	−0.966	−0.408	0.407	0.614	0.428	0.852
1.11	2.241	0.264	−0.251	−0.253	6.582	−0.008	−1.026	0.071	−0.964	−0.319	0.396	0.605	0.426	0.839
1.18	2.269	0.212	−0.251	−0.290	6.079	−0.008	−1.022	0.075	−0.957	−0.283	0.391	0.599	0.428	0.834
1.26	2.500	0.014	−0.266	−0.375	5.964	−0.008	−1.016	0.080	−0.972	−0.296	0.396	0.598	0.427	0.835
1.34	2.491	0.058	−0.255	−0.363	6.148	−0.008	−1.005	0.087	−0.999	−0.332	0.399	0.595	0.425	0.833
1.42	2.433	0.088	−0.245	−0.346	6.435	−0.009	−0.991	0.092	−1.006	−0.326	0.398	0.595	0.425	0.832
1.51	2.335	0.192	−0.231	−0.294	7.106	−0.009	−0.971	0.091	−1.004	−0.289	0.400	0.592	0.426	0.832
1.61	2.274	0.266	−0.220	−0.260	7.708	−0.009	−0.946	0.089	−1.003	−0.289	0.400	0.587	0.427	0.829

(*continued*)

Table 1. (*continued*)

f (Hz)	c_0	c_1	c_2	c_3	c_4	c_5	c_6	c_7	b_1	b_2	τ	ϕ_{S2S}	ϕ_{SS}	σ
1.71	2.277	0.277	−0.216	−0.258	7.951	−0.010	−0.931	0.090	−1.003	−0.281	0.396	0.579	0.432	0.824
1.82	2.195	0.353	−0.206	−0.221	7.688	−0.010	−0.929	0.090	−1.007	−0.277	0.396	0.571	0.435	0.820
1.93	2.074	0.445	−0.193	−0.161	7.641	−0.010	−0.931	0.087	−1.010	−0.304	0.401	0.562	0.435	0.816
2.06	1.951	0.511	−0.179	−0.116	7.761	−0.010	−0.921	0.088	−1.014	−0.316	0.398	0.557	0.436	0.811
2.19	1.914	0.506	−0.173	−0.118	7.759	−0.010	−0.904	0.094	−1.023	−0.339	0.399	0.557	0.436	0.812
2.33	1.796	0.596	−0.159	−0.081	7.731	−0.010	−0.878	0.097	−1.027	−0.338	0.394	0.557	0.435	0.809
2.48	1.620	0.764	−0.138	0.021	8.044	−0.011	−0.853	0.093	−1.030	−0.339	0.393	0.557	0.438	0.810
2.63	1.627	0.754	−0.137	0.053	8.596	−0.011	−0.844	0.088	−1.032	−0.369	0.396	0.555	0.443	0.813
2.8	1.668	0.681	−0.141	0.020	8.649	−0.011	−0.839	0.091	−1.031	−0.379	0.399	0.553	0.448	0.816
2.98	1.714	0.588	−0.145	−0.044	8.305	−0.011	−0.829	0.098	−1.028	−0.362	0.400	0.554	0.452	0.819
3.17	1.888	0.371	−0.161	−0.156	7.956	−0.012	−0.815	0.107	−1.029	−0.348	0.394	0.553	0.454	0.817
3.37	1.841	0.330	−0.158	−0.159	7.829	−0.012	−0.798	0.111	−1.031	−0.336	0.390	0.555	0.454	0.816
3.58	1.452	0.578	−0.126	−0.015	8.106	−0.013	−0.773	0.111	−1.024	−0.314	0.392	0.562	0.454	0.822
3.81	1.002	0.941	−0.085	0.165	8.442	−0.013	−0.734	0.112	−1.022	−0.286	0.401	0.570	0.454	0.832
4.06	0.934	0.998	−0.077	0.181	8.458	−0.014	−0.694	0.114	−1.025	−0.299	0.405	0.574	0.453	0.836
4.31	0.979	0.944	−0.080	0.158	8.584	−0.014	−0.674	0.112	−1.028	−0.327	0.409	0.580	0.456	0.843
4.59	0.896	1.012	−0.072	0.197	9.058	−0.014	−0.659	0.110	−1.034	−0.355	0.417	0.591	0.457	0.855
4.88	0.739	1.128	−0.057	0.248	9.437	−0.014	−0.634	0.112	−1.039	−0.399	0.425	0.601	0.456	0.866
5.19	0.843	1.001	−0.068	0.166	9.286	−0.014	−0.601	0.119	−1.042	−0.426	0.432	0.611	0.454	0.876
5.52	0.954	0.850	−0.079	0.081	8.920	−0.014	−0.555	0.125	−1.042	−0.446	0.442	0.624	0.453	0.888
5.87	0.847	0.866	−0.072	0.105	9.017	−0.014	−0.510	0.128	−1.045	−0.480	0.450	0.636	0.452	0.901
6.25	0.650	0.943	−0.059	0.161	9.065	−0.015	−0.468	0.129	−1.042	−0.513	0.455	0.642	0.452	0.908
6.64	0.396	1.085	−0.040	0.248	8.990	−0.015	−0.428	0.126	−1.040	−0.524	0.459	0.650	0.453	0.916
7.07	0.258	1.154	−0.031	0.298	9.245	−0.015	−0.402	0.124	−1.047	−0.542	0.461	0.661	0.454	0.925
7.52	0.237	1.109	−0.032	0.283	9.163	−0.015	−0.375	0.127	−1.055	−0.556	0.470	0.672	0.457	0.939
7.99	0.201	1.043	−0.035	0.262	8.830	−0.015	−0.340	0.130	−1.055	−0.572	0.487	0.682	0.460	0.956
8.5	0.208	0.938	−0.043	0.219	8.527	−0.016	−0.301	0.132	−1.053	−0.577	0.495	0.695	0.463	0.971
9.05	0.210	0.859	−0.048	0.193	8.401	−0.016	−0.265	0.133	−1.058	−0.583	0.504	0.711	0.470	0.990
9.62	0.100	0.875	−0.043	0.207	8.493	−0.016	−0.241	0.133	−1.068	−0.611	0.518	0.729	0.476	1.013
10.23	−0.210	1.072	−0.021	0.306	8.616	−0.016	−0.220	0.131	−1.075	−0.632	0.530	0.746	0.484	1.035
10.88	−0.591	1.328	0.006	0.434	8.345	−0.016	−0.191	0.127	−1.078	−0.632	0.540	0.759	0.493	1.054
11.58	−0.794	1.412	0.017	0.498	8.048	−0.017	−0.156	0.124	−1.084	−0.641	0.548	0.775	0.501	1.074
12.31	−0.875	1.420	0.019	0.533	8.064	−0.017	−0.120	0.119	−1.099	−0.678	0.557	0.794	0.510	1.096
13.1	−1.088	1.533	0.031	0.611	7.970	−0.016	−0.088	0.112	−1.109	−0.723	0.566	0.812	0.520	1.118
13.93	−1.329	1.679	0.043	0.689	7.800	−0.016	−0.074	0.105	−1.113	−0.752	0.576	0.826	0.532	1.139
14.82	−1.498	1.763	0.047	0.750	7.731	−0.016	−0.064	0.093	−1.115	−0.804	0.586	0.838	0.548	1.160
15.76	−1.595	1.805	0.045	0.793	7.799	−0.016	−0.048	0.079	−1.119	−0.881	0.595	0.850	0.567	1.182
16.77	−1.687	1.842	0.043	0.831	7.664	−0.015	−0.037	0.065	−1.128	−0.951	0.600	0.859	0.587	1.201
17.83	−1.733	1.821	0.036	0.865	7.773	−0.015	−0.043	0.050	−1.139	−0.994	0.606	0.869	0.606	1.220
18.97	−1.767	1.828	0.033	0.904	8.260	−0.015	−0.048	0.038	−1.165	−1.028	0.616	0.880	0.625	1.243
20.17	−1.781	1.859	0.032	0.937	8.712	−0.014	−0.041	0.028	−1.201	−1.086	0.629	0.891	0.644	1.267
21.46	−1.894	1.903	0.034	0.984	8.894	−0.014	−0.043	0.016	−1.220	−1.152	0.638	0.904	0.664	1.290
22.83	−2.165	1.999	0.043	1.067	9.025	−0.013	−0.060	0.004	−1.229	−1.214	0.645	0.916	0.686	1.314
24.28	−2.569	2.144	0.058	1.191	8.974	−0.013	−0.079	−0.010	−1.229	−1.259	0.656	0.930	0.712	1.343
25.82	−2.858	2.272	0.067	1.315	8.436	−0.012	−0.041	−0.031	−1.225	−1.340	0.680	0.938	0.740	1.375
27.47	−2.910	2.159	0.053	1.284	8.269	−0.012	−0.033	−0.046	−1.213	−1.364	0.697	0.950	0.767	1.406
29.22	−2.921	1.994	0.034	1.196	8.145	−0.011	−0.039	−0.057	−1.205	−1.379	0.723	0.967	0.797	1.446

(*continued*)

Table 1. (*continued*)

f (Hz)	c_0	c_1	c_2	c_3	c_4	c_5	c_6	c_7	b_1	b_2	τ	ϕ_{S2S}	ϕ_{SS}	σ
31.08	−2.894	1.829	0.014	1.114	8.091	−0.011	−0.042	−0.065	−1.219	−1.432	0.742	0.983	0.826	1.483
33.05	−3.069	1.796	0.012	1.138	8.078	−0.010	−0.052	−0.073	−1.233	−1.482	0.745	1.000	0.855	1.512
35.16	−3.218	1.750	0.007	1.145	8.321	−0.010	−0.071	−0.082	−1.244	−1.526	0.756	1.021	0.883	1.548
37.39	−3.396	1.767	0.006	1.176	8.778	−0.009	−0.084	−0.095	−1.257	−1.592	0.774	1.050	0.910	1.590
39.78	−3.807	1.960	0.023	1.300	9.213	−0.008	−0.090	−0.109	−1.265	−1.641	0.792	1.081	0.938	1.636
42.31	−4.201	2.174	0.047	1.434	9.900	−0.007	−0.039	−0.118	−1.296	−1.705	0.826	1.075	0.921	1.639
45	−4.200	1.864	0.013	1.186	9.847	−0.006	−0.121	−0.088	−1.332	−1.723	0.864	1.124	0.963	1.714

site-specific between-station, and remaining path-specific components. The between-event residuals are believed to capture the source-related variations, while the between-station residuals capture the station-to-station variability in recorded ground motion with respect to the median model. Similarly, the single-station within-event residuals (ε) represent the path-specific variations. The three types of residuals are analyzed in Figures 3–6. Figure 3 shows a variation of between-event residuals (η_e) against magnitude at $f = 0.32$, 0.5, 3.17, 3.37, 5.19, and 10.23 Hz. η_e are shown using different markers to segregate them according to events from different regions. Between-event residuals are expected to capture the source-specific variations, such as the stress parameter and radiation pattern. Although our dataset is mainly populated by events from CA, we do not observe a clear regional pattern in between-event residuals. Figure 4 depicts the variation of between-event residuals against the style of faulting and depth to the top of the

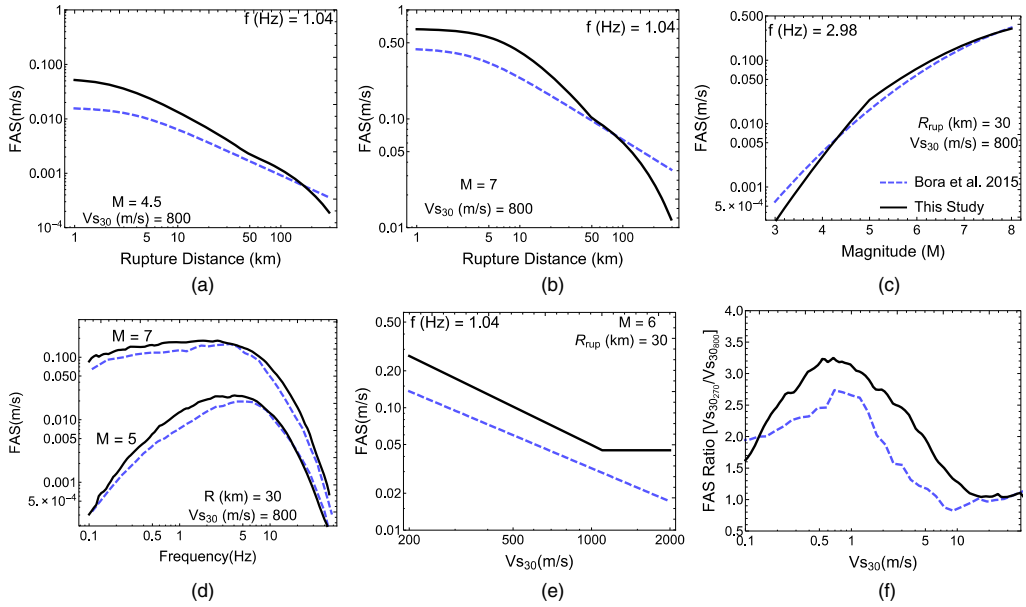

Figure 2. FAS model predictions and comparisons with Bora et al. (2015): (a) Distance scaling for **M**4.5, (b) distance scaling for **M**7, (c) magnitude scaling, (d) full spectra for **M**5 and **M**7, (e) V_{S30} scaling, and (f) FAS ratios: $V_{S30} = 270$ to 800 m/s.

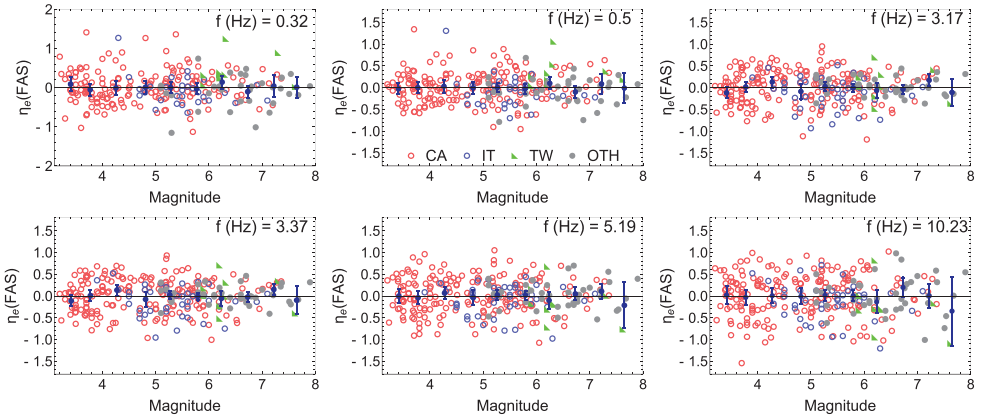

Figure 3. Between-event FAS residuals (η_e) against magnitude for events from CA, IT, TW, and OTH at frequencies $f = 0.32$, 0.5, 3.17, 3.37, 5.19, and 10.23 Hz. The dots with vertical bars indicate mean residuals with 95% confidence-intervals of the mean in 0.5 magnitude bins.

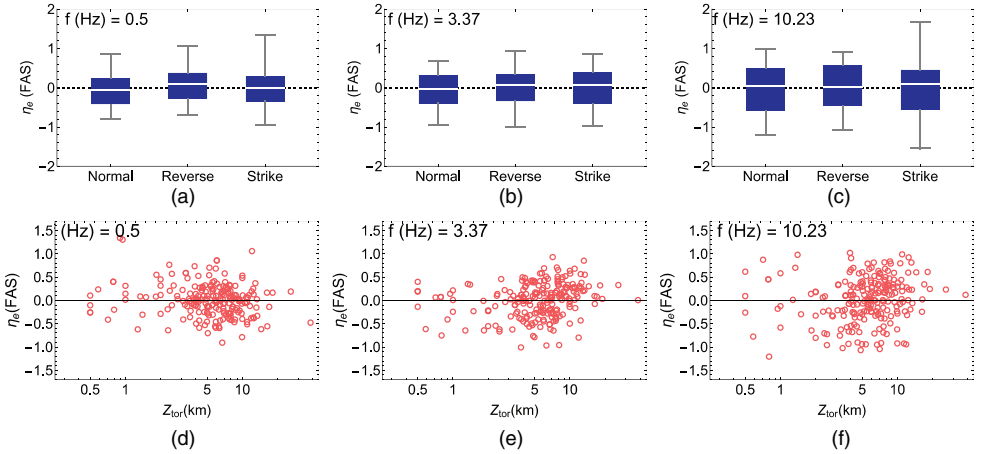

Figure 4. Between-event FAS residuals (η_e) against (a, b, c) the style of faulting and (d, e, f) Z_{tor} (depth to the top of the rupture) at frequencies $f = 0.5$, 3.37, and 10.23 Hz.

rupture Z_{tor}. We do not observe a clear dependence of between-event residuals over style of faulting and Z_{tor}, though they were not included in our median model.

The between-station residuals (η_s) are plotted against station V_{S30} values in Figure 5 at frequencies $f = 0.5$, 5.19, and 10.23 Hz. The between-station residuals are plotted separately for the different regions: CA, Japan, IT, and TW. The selected linear-site response model is seen performing well in all four regions, except that we do not have many stations from IT and TW in our dataset. We also investigated the variation of η_s with respect to $Z_{1.0}$ (depth to the layer with a velocity of 1 km/s). The plots of η_s against $Z_{1.0}$ are shown in Figures 6 and 7 for CA

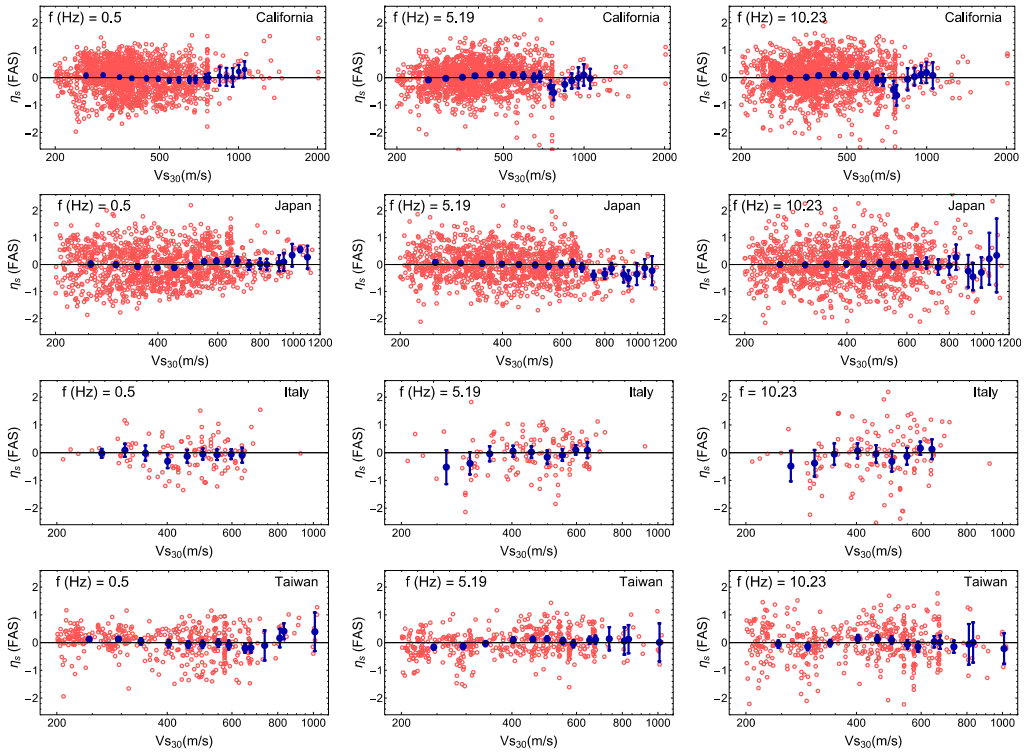

Figure 5. Between-station FAS residuals (η_s) against station V_{S30} values separated in four regions, CA, Japan, IT, and TW, at $f = 0.5$, 5.19, and 10.23 Hz. The dots with vertical bars indicate mean residuals with 95% confidence-intervals of the mean in 100 m/s V_{S30} bins.

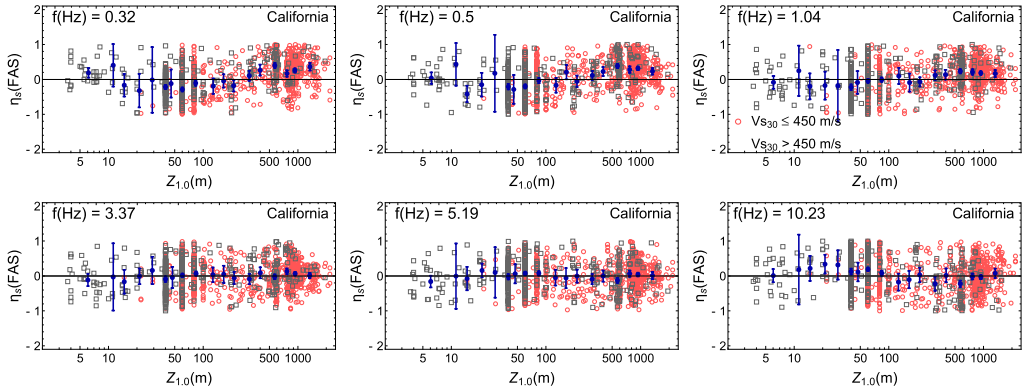

Figure 6. Between-station FAS residuals (η_s) against station $Z_{1.0}$ values for CA. The dots with vertical bars indicate mean residuals with 95% confidence-intervals of the mean in log-spaced depth bins.

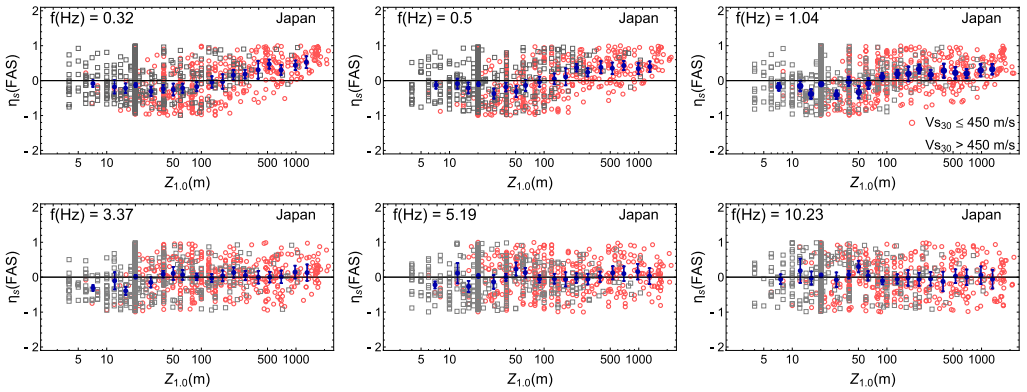

Figure 7. Between-station FAS residuals (η_s) against station $Z_{1.0}$ values for Japan. The dots with vertical bars indicate mean residuals with 95% confidence-intervals of the mean in log-spaced depth bins.

and Japan, respectively. The residuals show a clear dependence at lower frequencies ($\leq$1 Hz) for $Z_{1.0}$ larger than 110 m, but at higher frequencies the residuals are near zero. Also, the trend at lower frequencies is relatively stronger for Japan, indicating stronger basin effects.

The event and station-corrected (or single-station) residuals (ε) are plotted against distance at frequencies in $f = 0.5$, 5.19, and 10.23 Hz in Figure 8. Such residuals are expected to represent the variability in path characteristics (e.g., anelastic attenuation) of the recorded ground motion. To investigate the regional variations in anelastic attenuation, the residuals are plotted separately for the four different regions, CA, Japan, IT, and TW. From Figure 8, it can be noted that the selected distance scaling function also performs well in all four regions. Also, we do not observe a clear regional variation with respect to the median model, though the near distance scaling up to 20–30 km for TW appears to be slightly different than that for other regions. Our dataset is quite limited in the terms of recordings from IT and TW at longer distances.

RVT AND DURATION ESTIMATION

The other important element of our approach is an empirical model for the duration of ground motion. Multiple definitions of ground motion duration are available in literature, and the choice of a particular type is mainly driven by its suitability for a specific application (Bommer and Martínez-Pereira 1999). For the present analysis, we adopt the same definition of ground motion duration as used in Bora et al. (2015). This measure of duration is different from other measures of duration in that it is not determined directly from an acceleration trace as a time interval between certain levels of amplitude (bracketed duration) or arias intensity (significant duration). It is determined within the RVT framework by using the actual response spectral ordinates, i.e., Pseudo Spectral Acceleration (PSA) values, and the observed FAS of an acceleration trace. In this section, first we describe the relevant equations

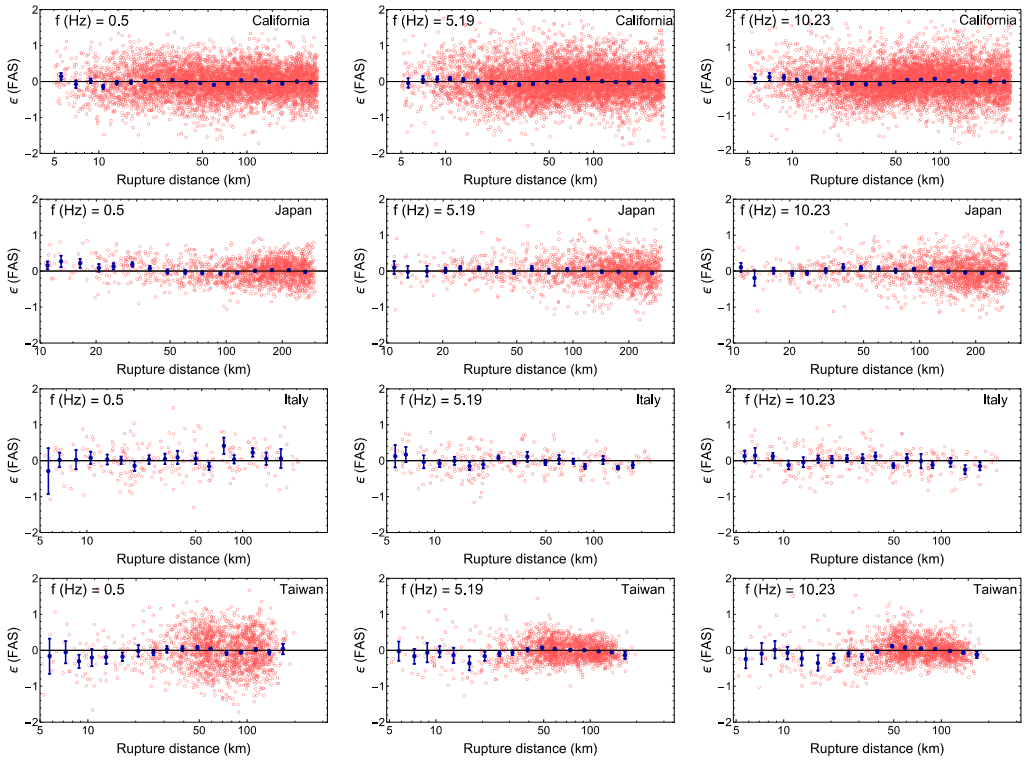

Figure 8. Single-station within-event FAS residuals (ε) against distance seperated in four regions, CA, Japan, IT, and TW, at $f = 0.5$, 5.19, and 10.23 Hz. The dots with vertical bars indicate mean residuals with 95% confidence-intervals of the mean in equally spaced (in log) distance bins.

involved in RVT computation and then how the duration is estimated from the recorded acceleration traces within the RVT framework.

As mentioned in the *Introduction* section of this article, the computation of response spectral amplitudes, PSA in this case, through RVT requires both the FAS and duration of ground motion. D. M. Boore has shown successfully that RVT provides a faster technique to compute response spectral amplitudes in his landmark stochastic simulation paper (Boore 2003). Within RVT, a PSA ordinate $y_{\max}$ at an oscillator frequency f_{osc} of an SDOF oscillator with damping ratio ζ is related to the root-mean-square motion, y_{rms}, through a peak factor, which is a function of the spectral moments and the duration D as follows:

$$\frac{y_{\max}(f_{\mathrm{osc}},\zeta)}{y_{\mathrm{rms}}(f_{\mathrm{osc}},\zeta)} = \sqrt{2}\int_0^{\infty}\left\{1-[1-\xi\exp(-z^2)]^{N_e}\right\}\mathrm{d}z \tag{7}$$

where

$$\xi(f_{\mathrm{osc}},\zeta)=\frac{m_2}{\sqrt{m_0 m_4}}, \tag{8}$$

and the number of extrema N_e is given by the following:

$$N_e(f_{\mathrm{osc}},\zeta)=\frac{1}{\pi}\sqrt{\frac{m_4}{m_2}}\mathrm{D}. \tag{9}$$

The spectral moments (m_k, $k=0, 2, 4$) at each f_{osc} are computed from the FAS of the response of an SDOF system as follows:

$$m_k(f_{\mathrm{osc}},\zeta)=2\int_0^{\infty}(2\pi f)^k\,|Y_{\mathrm{SDOF}}(f,f_{\mathrm{osc}},\zeta)|^2\mathrm{d}f. \tag{10}$$

In Equation 10, the $|Y_{\mathrm{SDOF}}(f,f_{\mathrm{osc}},\zeta)|^2$ is obtained by multiplying the square of the ground motion Fourier spectrum $|Y_{\mathrm{gm}}(f)|^2$ with the squared SDOF transfer function, $|I(f,f_{\mathrm{osc}}\zeta)|^2$, as follows:

$$|Y_{\mathrm{SDOF}}(f,f_{\mathrm{osc}},\zeta)|^2=|Y_{\mathrm{gm}}(f)|^2\,|I(f,f_{\mathrm{osc}}\zeta)|^2, \tag{11}$$

where the SDOF transfer function, $|I(f,f_{\mathrm{osc}},\zeta)|$, is defined as in the following equation:

$$|I(f,f_{\mathrm{osc}},\zeta)|=\frac{f_{osc}^2}{\sqrt{(f^2-f_{\mathrm{osc}}^2)^2+(2ff_{\mathrm{osc}}\zeta)^2}}. \tag{12}$$

Note that the Y_{gm} in Equation 11 is acceleration motion. The y_{rms} is given by the following equation:

$$y_{rms}(f_{osc},\zeta)=\sqrt{\frac{m_0}{D}} \tag{13}$$

Thus, it can be noted from Equations 7–13 that to obtain PSA using the RVT technique, one needs two quantities, i.e., the FAS and duration of ground motion. In order to determine the duration from the acceleration traces, we treat it as a variable (in the RVT formulation) to minimize the mismatch between the actual PSA and that obtained through RVT as a combination of the actual FAS and the duration (to be determined). Essentially, a squared mismatch (in log space) is minimized at each oscillator frequency to get an oscillator frequency–dependent duration that we call random-vibration theory optimized duration (D_{rvto}). In our analysis, hereafter we refer to the duration as D_{rvto}. Note that we do not use a different measure of duration, i.e., a root-mean-square duration (D_{rms}) for computing y_{rms}. Also note that we determine D_{rvto} for 5% of critical damping; that is, $\zeta=0.05$. The lower limit of the useable oscillator frequency was fixed at a frequency that is 1.25 times of the high-pass frequency corresponding to each trace.

FREQUENCY-DEPENDENT DURATION MODEL

In our approach of obtaining response spectral ordinates, we need two models, one for the FAS and the other for the duration of ground motion. The most recent predication equations for the duration are from Kempton and Stewart (2006), Bommer et al. (2009), Lee and Green (2014), Bora et al. (2014, 2015), Afshari and Stewart (2016), and Sandıkkaya and Akkar (2017). Except for Afshari and Stewart (2016), none of them is calibrated on the NGA-West2 database. The Afshari and Stewart (2016) model predicts a constant (frequency-independent) significant duration. Physically, the source duration is often related to the reciprocal of the source-corner frequency. However, the physics of the path effects is not yet clear, which is assumed to be mainly arising from the dispersion and scattering of traveling seismic waves. Thus, to select a functional form for the duration model, many preliminary regressions and visual checks were performed. Similar to Bommer et al. (2009) and Bora et al. (2014, 2015), we selected a functional form for D_{rvto} as follows:

$$\log D_{rvto}(f_{osc}) = d_0 + F_e(\mathbf{M}) + F_p(R_{rup}, \mathbf{M}) + F_s(V_{S30}) + \eta_e + \eta_s + \varepsilon \tag{14}$$

In the above equation, F_e, F_p, and F_s are the source, path, and site functions, respectively, and the definitions of the predictor variables ($\mathbf{M}$, R_{rup}, V_{S30}) and the residual terms ($\eta_e, \eta_s, \varepsilon$) remain the same as in Equation 1.

The source function F_e is given as follows:

$$F_e = \begin{cases} d_1\mathbf{M} & \mathbf{M} \le 5.3 \\ d_1\mathbf{M} + d_2(M - 5.3) & \mathbf{M} > 5.3 \end{cases} \tag{15}$$

The break in the magnitude scaling function at $\mathbf{M} = 5.3$ was based upon our preliminary regression checks. Afshari and Stewart (2016) have also observed a break in the magnitude scaling of duration at **M**5.2.

The path function F_p is given by the following equation:

$$F_p = (d_3 + d_4(\mathbf{M} - 6)) \log R_{rup} \tag{16}$$

We clearly observed a magnitude-dependent distance scaling of duration with a steeper (stronger) distance-dependence for smaller-magnitude events in comparison to that for larger magnitudes. In Equation 16, the reference magnitude of **M**6 was based upon visual inspection of the data in our preliminary analysis.

The site function F_s is given as follows:

$$F_s = \begin{cases} d_5 \log(V_{S30}) & V_{S30} \le 450 \text{ m/s} \\ d_5 \log(450) & V_{S30} > 450 \text{ m/s} \end{cases} \tag{17}$$

A rather weak V_{S30} dependence of D_{rvto} was observed until $V_{S30} = 400$–500 m/s, and beyond that it was observed to be almost independent of V_{S30}.

The coefficients of the regression model, that is, Equations 14–17, were again determined by mixed-effects regression algorithm. A frequency-by-frequency regression was performed

Table 2. Coefficients associated with empirical duration (D_{rvto}) model (Equations 14–17)

f_{osc} (Hz)	d_0	d_1	d_2	d_3	d_4	d_5	τ	ϕ_{S2S}	ϕ_{SS}	σ
0.1	−12.453	2.265	2.344	0.624	−0.403	−0.027	0.754	0.241	0.494	0.933
0.2	−6.520	1.690	1.535	0.482	−0.310	−0.287	0.613	0.244	0.522	0.841
0.25	−5.009	1.480	1.322	0.454	−0.279	−0.310	0.474	0.270	0.525	0.757
0.33	−2.608	1.186	1.045	0.394	−0.230	−0.388	0.391	0.283	0.524	0.713
0.4	−1.543	1.036	0.895	0.357	−0.202	−0.404	0.327	0.298	0.517	0.681
0.5	0.334	0.723	0.733	0.328	−0.160	−0.424	0.265	0.299	0.503	0.642
1	3.352	0.196	0.314	0.322	−0.062	−0.462	0.203	0.266	0.455	0.565
2	2.543	0.110	0.423	0.333	−0.060	−0.342	0.193	0.260	0.452	0.557
2.94	1.765	0.134	0.577	0.347	−0.073	−0.297	0.200	0.246	0.456	0.556
3.33	1.514	0.145	0.633	0.351	−0.079	−0.285	0.205	0.244	0.459	0.558
4	1.124	0.172	0.700	0.365	−0.085	−0.272	0.208	0.249	0.463	0.565
5	0.746	0.171	0.757	0.379	−0.089	−0.238	0.234	0.262	0.463	0.581
7.52	−0.299	0.287	0.918	0.433	−0.113	−0.229	0.249	0.284	0.470	0.603
10	−0.684	0.335	1.032	0.471	−0.128	−0.248	0.255	0.297	0.479	0.618
14.92	−0.902	0.413	1.103	0.485	−0.147	−0.293	0.272	0.309	0.495	0.644
20	−0.597	0.390	1.079	0.478	−0.141	−0.316	0.275	0.325	0.507	0.662
25	−0.433	0.383	1.070	0.471	−0.140	−0.332	0.283	0.328	0.514	0.672
33.33	−0.309	0.393	1.073	0.477	−0.143	−0.369	0.285	0.328	0.522	0.679
50	−0.256	0.415	1.066	0.485	−0.139	−0.409	0.294	0.332	0.514	0.679
100	−0.472	0.479	1.080	0.493	−0.145	−0.437	0.297	0.333	0.513	0.680

at twenty oscillator frequencies in the range 0.1–100 Hz. The model coefficients and corresponding standard deviations are listed in Table 2.

DURATION (D_{rvto}) MODEL PREDICTION

Median predictions from our D_{rvto} model are depicted in Figure 9; we have also shown D_{rvto} predictions from Bora et al. (2015) for comparison. As we use the same measure of ground motion duration, that is, D_{rvto}, in the two studies, such comparisons should be useful in evaluating regional variations in the ground motion duration between the two underlying datasets NGA-West2 and RESORCE-2012. Figure 9a depicts the distance scaling of D_{rvto} at $f_{osc} = 100$ Hz. The shape of the distance scaling of D_{rvto} is also different between the two models, mainly due to the different functional forms adopted. Figure 9b and 9c depicts the magnitude scaling of D_{rvto} at $f_{osc} = 1$ and 100 Hz, respectively. From this study, the break in magnitude scaling at **M**5.3 is quite evident, while the study done by Bora et al. (2015) does not exhibit such a transition. Figure 9d shows a variation of D_{rvto} over the entire oscillator frequency range corresponding to different V_{S30} values for both the models. A weaker dependence of D_{rvto} over V_{S30} is evident in both the models. In general, D_{rvto} values from this study are significantly larger than the values from Bora et al. (2015). Such differences are mainly due to (1) the differences in underlying datasets, that is, NGA-West2 and RESORCE-2012, and (2) the differences in the selected functional forms for the two empirical models.

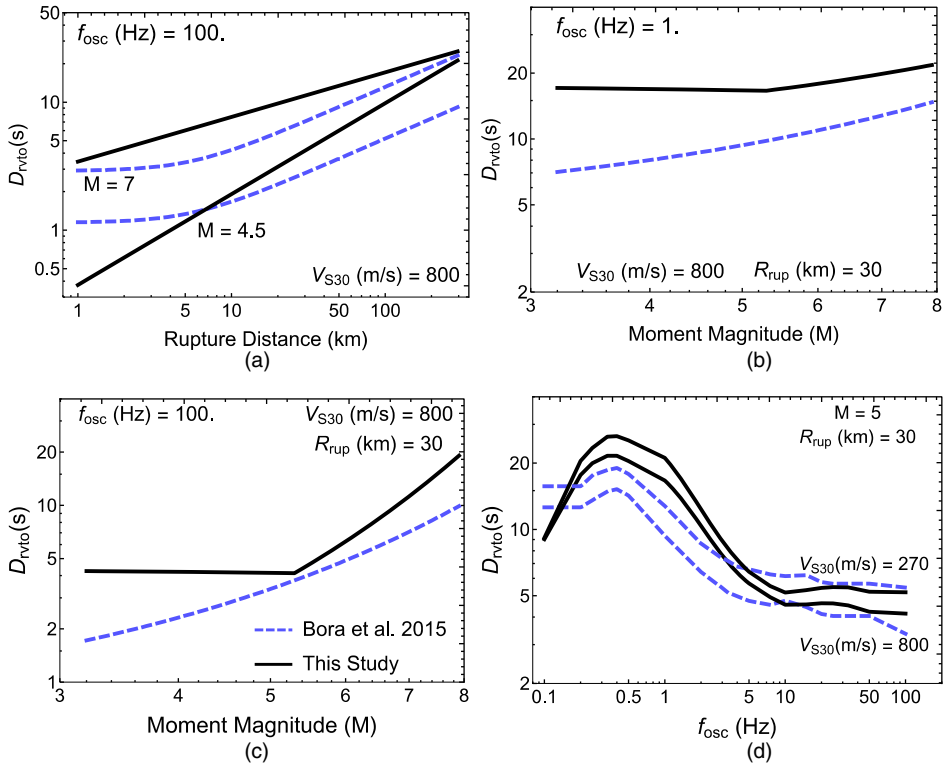

Figure 9. D_{rvto} model predictions and comparisons with Bora et al. (2015): (a) Distance scaling for **M**4.5 and **M**7, (b) magnitude scaling at $f_{osc} = 1$ Hz, (c) magnitude scaling at $f_{osc} = 100$ Hz, and (d) variation over entire oscillator frequency range for V_{S30} 270 and 800 m/s.

RESIDUALS

Similar to our analysis for the FAS model, we performed a mixed-effects regression involving Equations 14–17 using the entire dataset. In our regression algorithm, we separated event-specific, station-specific, and path-specific effects in between-event (η_e), between-station (η_s), and single-station within-event residuals (ε), respectively. Between-event residuals are analyzed in Figures 10 and 11. Figure 10 depicts a variation of η_e against the magnitude, separated according to the events from CA, IT, TW, and the remaining events (OTH), though we did not observe any regional pattern in the residuals. The selected magnitude scaling function can be seen in reasonably good agreement with the data. However, a larger variability at smaller oscillator frequencies $f_{osc} = 0.5$ Hz and towards a smaller magnitude is observed. To better understand the larger variability at smaller oscillator frequencies, we plot the η_e values against Z_{tor} at $f_{osc} = 0.25$, 0.33, 0.5, 1, 5, and 100 Hz in Figure 11. A rather stronger depth dependence of between-event residuals for smaller magnitudes can explain this larger variability at smaller oscillator frequencies, i.e., $f_{osc} = 0.25$, 0.33, and 0.5 Hz. Physically, smaller durations for deeper events can be attributed to (1) a larger stress parameter and (2) the lack of dispersion in path effects.

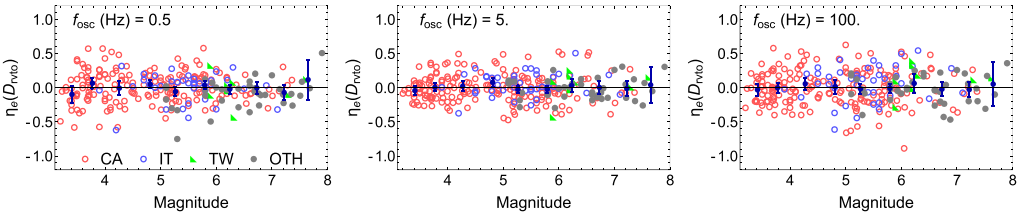

Figure 10. Between-event residuals (η_e) of D_{rvto} model against magnitude for events from CA, IT, TW, and OTH at oscillator frequencies $f_{osc} = 0.5$, 5, and 100 Hz. The dots with vertical bars indicate mean residuals with 95% confidence-intervals of the mean in 0.5 magnitude bins.

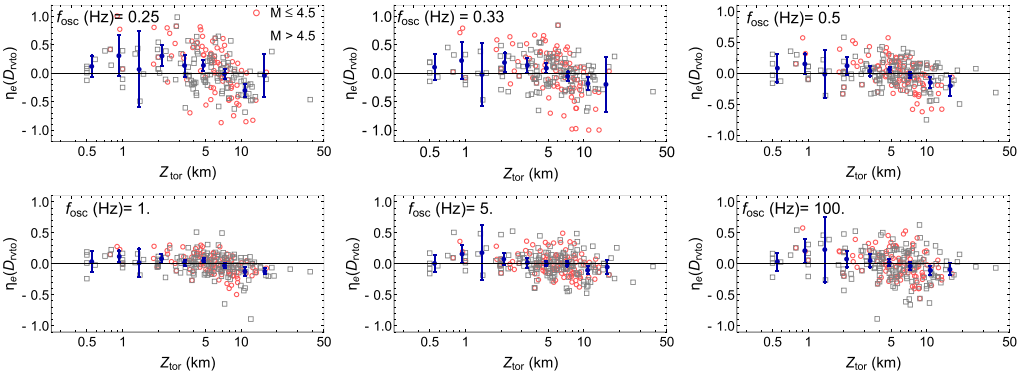

Figure 11. Between-event residuals (η_e) of D_{rvto} model against Z_{tor} at oscillator frequencies $f_{osc} = 0.25$, 0.33, 0.5, 1, 5, and 100 Hz. Empty circles and empty squares indicate the between-event residuals for smaller ($\mathbf{M} \leq 4.5$) and larger ($\mathbf{M} > 4.5$) magnitudes, respectively. The dots with vertical bars indicate mean residuals with 95% confidence-intervals of the mean in log-spaced depth bins.

Figure 12 shows the variation of between-station residuals against station V_{S30} values. Separate plots are shown for stations located in CA, Japan, IT, and TW. Since we do not observe regional patterns among the residuals, the selected V_{S30} scaling function is observed to be robust. To investigate the soil depth effects on the duration D_{rvto}, we also plotted the between-station residuals against $Z_{1.0}$ (depth to the layer with velocity 1 km/s). As shown in Figure 13, we observe a clear dependence of between-station residuals on $Z_{1.0}$, indicating longer durations for sites having deeper soil layers in Japan, while CA sites do not exhibit such dependence. Note that the plots in Figure 13 include only stations that are prescribed with the measured V_{S30}.

The single-station residuals are plotted in Figure 14 with separate plots for recordings made in CA, Japan, IT, and TW. The selected distance scaling function is also observed to be robust. However, one can observe a transition distance around 40–60 km in the distance scaling of the duration for CA. Although the majority of the records in our dataset are

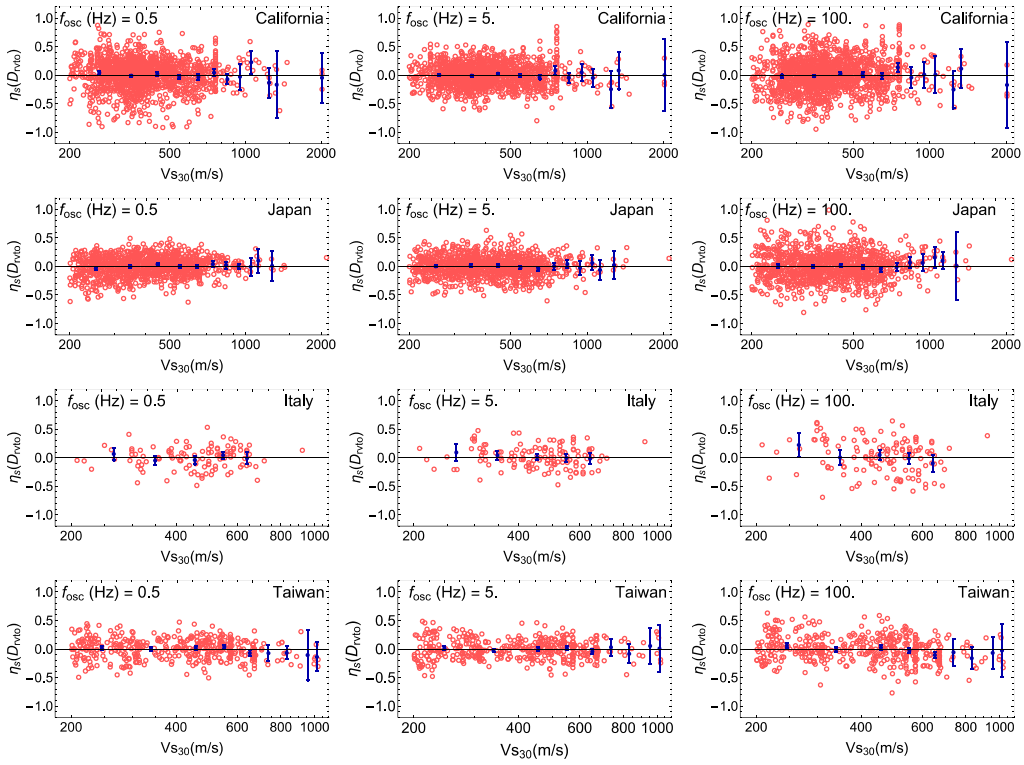

Figure 12. Between-station residuals (η_s) of D_{rvto} model against station V_{S30} values. Separated in four regions, CA, Japan, IT, and TW, at $f_{osc} = 0.5$, 5, and 100 Hz. The dots with vertical bars indicate mean residuals with 95% confidence-intervals of the mean in 100 m/s V_{S30} bins.

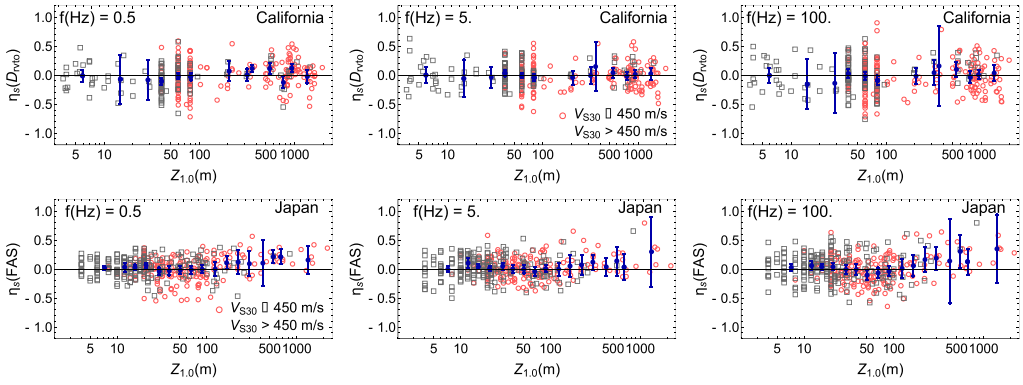

Figure 13. Between-station residuals (η_s) of D_{rvto} model against station $Z_{1.0}$ values. Separately plotted for Japan and CA at $f_{osc} = 0.5$, 5, and 100 Hz. The dots with vertical bars indicate mean residuals with 95% confidence-intervals of the mean in log-spaced depth bins.

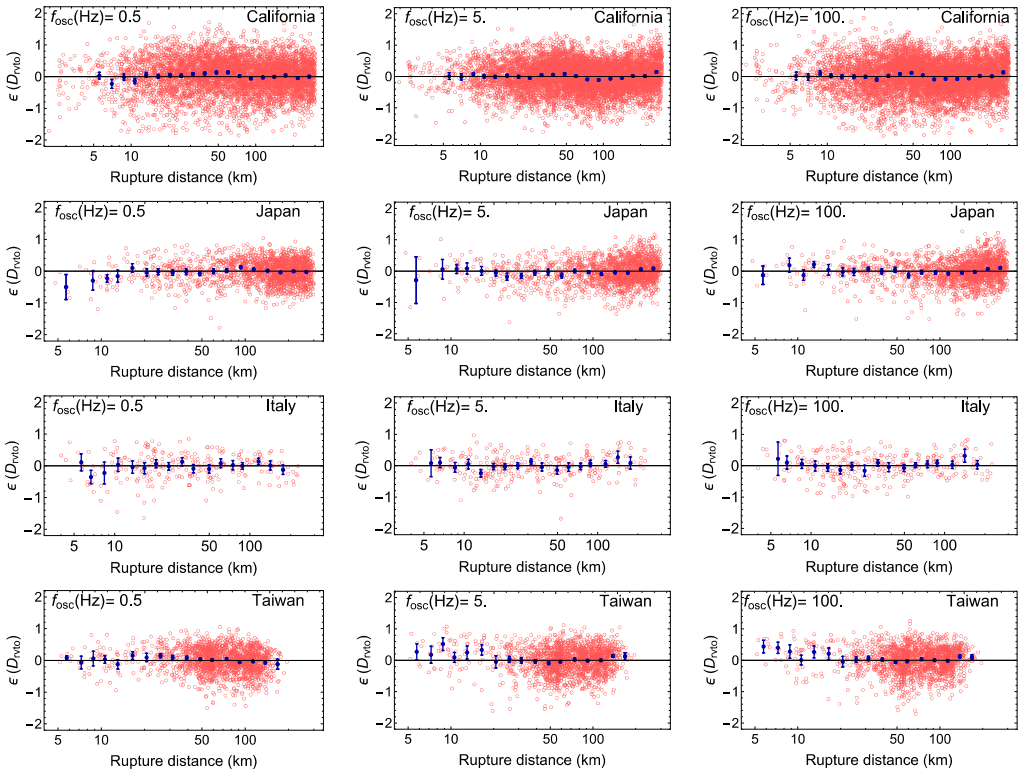

Figure 14. Single-station within-event residuals (ε) for D_{rvto} model against distance. Separated in four regions, CA, Japan, IT, and TW, at $f_{osc} = 0.5$, 5, and 100 Hz. The dots with vertical bars indicate mean residuals with 95% confidence-intervals of the mean in equally spaced (in log) distance bins.

from CA, Figure 14 also indicates that the selected distance scaling function can be suitable for predicting durations in the aforementioned regions. It is interesting to note that the near-distance D_{rvto} single-station within-event residuals (ε) for TW are slightly higher than the median, while the FAS single-station residuals in Figure 8 are lower than the median in the same near-distance range.

RESPONSE SPECTRA

As discussed earlier, our approach of obtaining response spectra (PSAs) consists of deriving two separate models: One for FAS and the other for a unique measure of ground motion duration D_{rvto}, which are subsequently combined within the RVT framework. The RVT procedure utilizes the mean values of FAS and duration; hence, the median predictions from Equations 1 and 14 should be converted to the corresponding mean values of FAS and D_{rvto}, respectively. Moreover, in our analysis (not shown in the manuscript) for Bora et al. (2015), we found the least variance and bias in PSA values by using the mean predictions of FAS and D_{rvto}. Thus, the median predictions obtained from the two empirical

models are converted to mean predictions, assuming that FAS at a given frequency and D_{rvto} at a given oscillator frequency follow log-normal distributions. The equations used for the conversion of mean from median prediction are as follows:

$$\ln[Y(f,\mathbf{M},R_{rup},V_{S30})_{mean}] = \ln Y(f,\mathbf{M},R_{rup},V_{S30}) + \frac{\tau^2+\phi_{S2S}^2+\phi_{SS}^2}{2} \quad (18)$$

$$\ln[D_{rvto}(f_{osc},\mathbf{M},R_{rup},V_{S30})_{mean}] = \ln D_{rvto}(f_{osc},\mathbf{M},R_{rup},V_{S30}) + \frac{\tau^2+\phi_{S2S}^2+\phi_{SS}^2}{2} \quad (19)$$

Essentially, for the forward prediction of PSA values, first we use Equations 1 and 14 to obtain the median predictions for FAS and D_{rvto}. Then the median predictions are converted to mean using Equations 18 and 19. Finally, the RVT framework, i.e., Equations 7–13, is employed to obtain the predicted PSA values. Note that the first term on the right-hand side in Equations 18 and 19 represents the corresponding median predictions for FAS and D_{rvto}, respectively.

Recently derived NGA-West2 GMPEs provide an excellent opportunity to evaluate the consistency of our approach of obtaining PSA values. A graphical comparison is performed between the present analysis and other selected NGA-West2 GMPEs. For this purpose, the ASK14, BSSA14, CB14, and CY14 GMPEs are selected. We have used Gregor et al. (2014) as a template for selecting our predictor variable scenarios to show comparisons.

DISTANCE SCALING

The median attenuation of PGA for horizontal ground shaking from our approach is compared with that from four NGA-West2 GMPEs in Figure 15. The plots are shown for $V_{S30} = 800\,\text{m/s}$. We have used the Joyner-Boore distance (R_{JB}) metric for the PSA comparisons. Median predictions from NGA-West2 models are computed for a vertical dipping striking slip event, and the $Z_{1.0}$ and $Z_{2.5}$ values are based on the recommended default values given for each GMPE (for ASK14 and CY14 $Z_{1.0} = 0.0481\,\text{km}$, and for CB $Z_{2.5} = 0.6068\,\text{km}$). For the BSSA14 model, the basin depth adjustment term $\delta z_1 = 0$ is used. Similar to Gregor et al. (2014), the depth to the top of the rupture was chosen to be magnitude dependent: **M**5 $Z_{tor} = 6\,\text{km}$, **M**6 $Z_{tor} = 3\,\text{km}$, **M**7 $Z_{tor} = 1\,\text{km}$, and **M**8 $Z_{tor} = 0\,\text{km}$. Overall, the PSA predictions from our approach can be seen to be in good agreement with those from the NGA-West2 GMPEs, except for **M**8. Note that none of the models are calibrated for an **M**8 event. The predictions for **M**5 are slightly higher than other models at near distances. However, a significant amount of epistemic uncertainty can also be observed amongst the NGA-West2 models. The same comparison of distance attenuation for $f_{osc} = 1\,\text{Hz}$ PSA is shown in Figure A1 (in online Appendix) for $V_{S30} = 270\,\text{m/s}$. The default values of the basin depth terms (for ASK14 and CY14 $Z_{1.0} = 0.4704\,\text{km}$, and for CB $Z_{2.5} = 1.982\,\text{km}$) are used. Similar to Figure 15, predictions from our approach are in good comparison with the other models for **M**5 and **M**6; however they are larger for **M**7 and **M**8. This is mainly due to the incorporated nonlinear site effects in the NGA-West2 models.

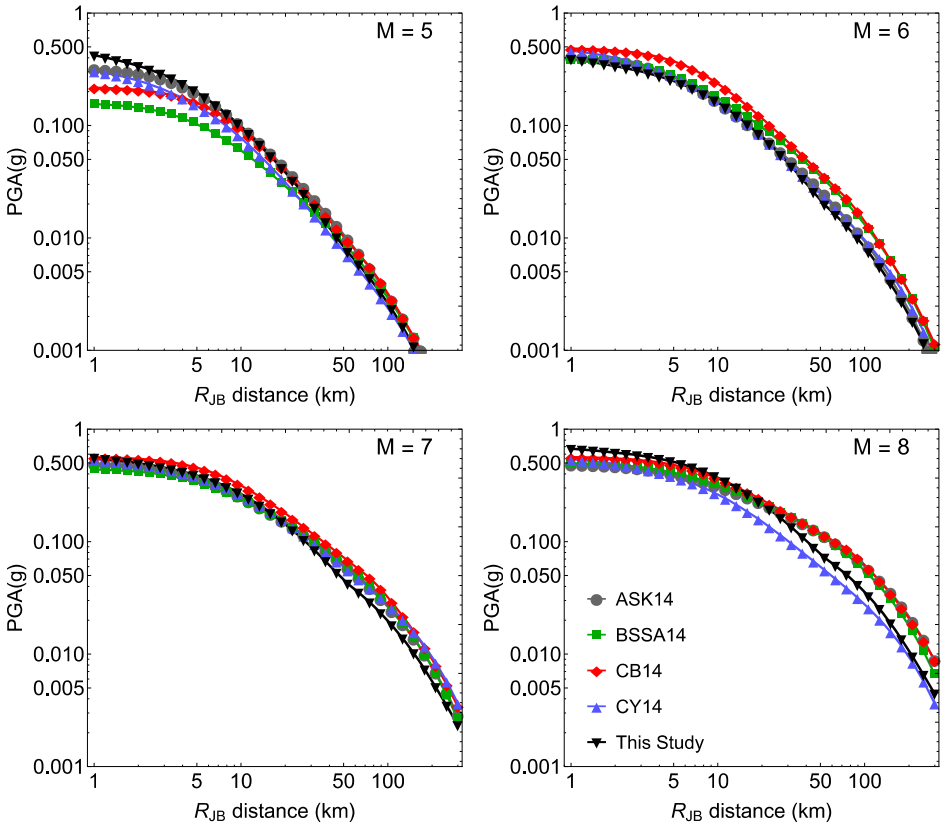

Figure 15. Comparisons of distance scaling of PGA for $V_{S30} = 800\,\mathrm{m/s}$. Predictions from NGA-West2 models are shown for strike-slip events.

MAGNITUDE SCALING

A comparison of magnitude scaling from our approach with other models is depicted in Figure 16. The plots are shown for vertical strike-slip events at $R_{JB} = 30\,\mathrm{km}$ for $V_{S30} = 800\,\mathrm{m/s}$. Plots are shown for PGA and $f_{osc} = 0.33$, 1, and 5 Hz. Note that the 100-Hz PSA value from our approach is used as the PGA. For the NGA-West2 models, the **M**-dependent depth to the top of the rupture (Z_{tor}) is computed by using the CY14 model. The default values of the basin depth parameters (ASK14 $Z_{1.0} = 0.0481\,\mathrm{km}$, and for CB14 $Z_{2.5} = 0.6068\,\mathrm{km}$) were used. The magnitude scaling of PSA from our approach can be seen to be in very good agreement with the other models.

V_{S30} SCALING

A comparison of median ground motion predictions as a function of V_{S30} is shown in Figures 17 and 18 for an **M**7 event at $R_{JB} = 100$ and 10 km, respectively. Predictions from the NGA-West2 GMPEs (ASK14, BSSA14, CB14, and CY14) are obtained for a vertical strike-slip event. The Z_{tor} was fixed at 1 km for the ASK14 and CB14 models. The default

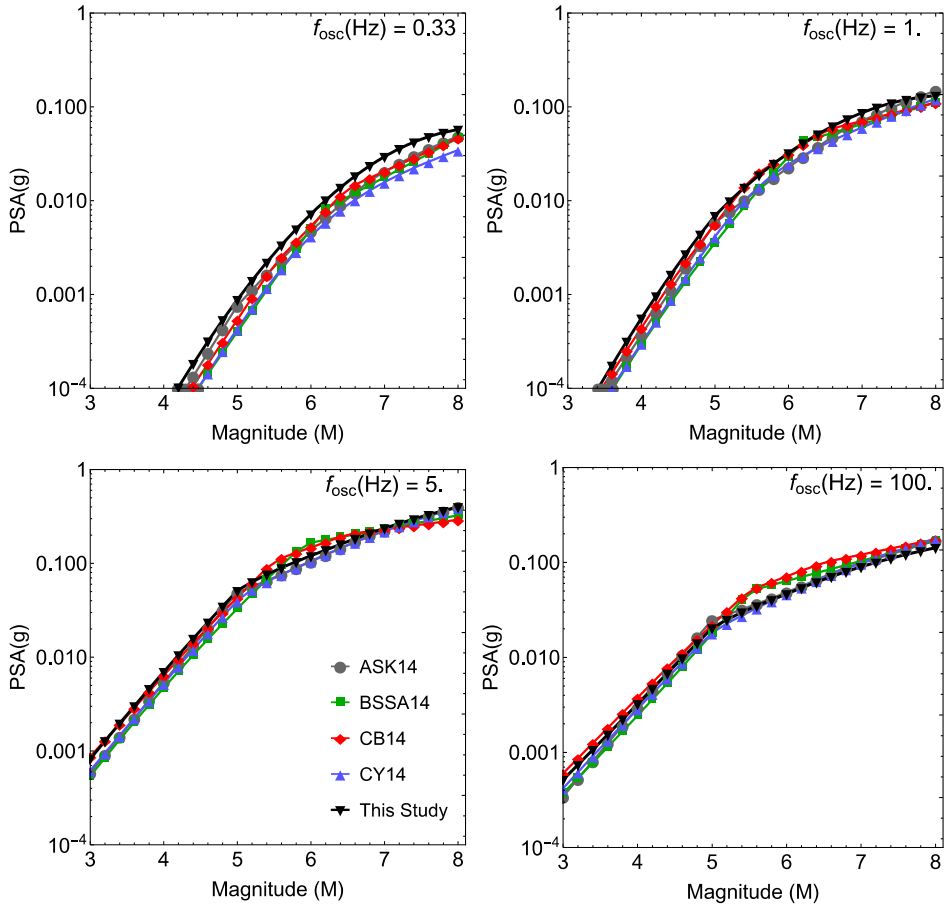

Figure 16. Comparison of magnitude scaling of the median predictions for $f_{osc} = 0.33$, 1, 5, and 100 Hz (PGA) at $R_{JB} = 30$ km and for $V_{S30} = 800$ m/s.

values of $Z_{1.0}$ and $Z_{2.5}$ were based on the respective relationship provided for each GMPE. At a 100-km distance, the median predictions clearly exhibit the choice of $V_c = 1{,}100$ m/s in this study. At a 100-km distance, the site amplification is almost linear, and V_{S30} scaling from our approach is in good agreement with the other models. At $R_{JB} = 10$ km (Figure 18) for $f_{osc} = 0.33$ Hz, our model predictions are similar to those from other models. With the increasing oscillator frequency, we see a strong impact of a nonlinear site response in the NGA-West2 models at smaller V_{S30} values. Note that, in the linear site-response domain, that is, $V_{S30} = 400$–$1{,}100$ m/s, the predictions from our model are similar to the other models.

RESPONSE SPECTRA

The response spectra from **M**5, 6, 7, and 8 earthquakes at a distance $R_{JB} = 10$ km are shown in Figure 19 for $V_{S30} = 800$ m/s. In Figure 19, the same default parameters (as used

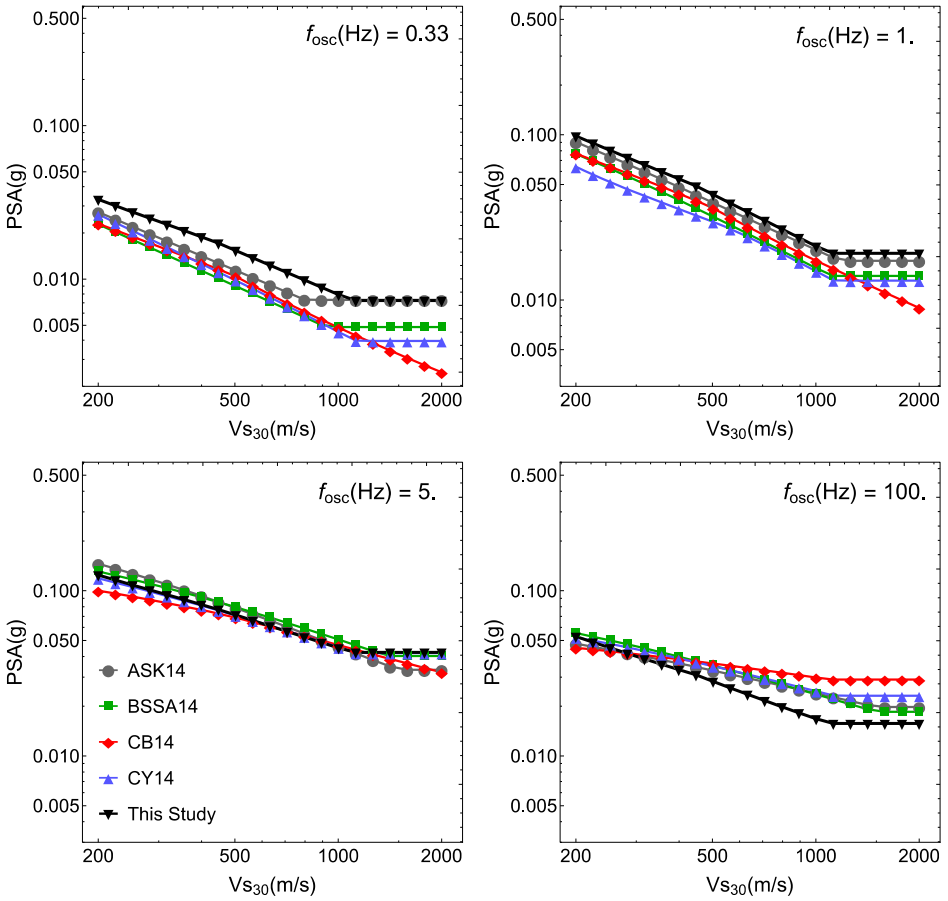

Figure 17. Comparison of V_{S30} scaling of the median predictions for an **M**7 earthquake at distance $R_{JB} = 100$ km.

for Figure 15) were used for the NGA-West2 GMPEs. Figure 19 indicates that the model predictions from this study are consistent with those from other models. The predictions from our model are in reasonably good comparison with other models, except our predictions are slightly higher for **M**5. Importantly, the response spectral shape from our analysis is quite similar to that from other models.

RESIDUALS AND ALEATORY VARIABILITY

We also provide an estimate of the aleatory variability involved in our approach of predicting response spectra. For this purpose, response spectral (total) residuals were first computed by subtracting the predicted log (natural) PSA values from the log of observed PSA values at each oscillator frequency, f_{osc}. The predicted PSA values were obtained through RVT by combining FAS and D_{rvto} predictions and using Equations 18 and 19. The total

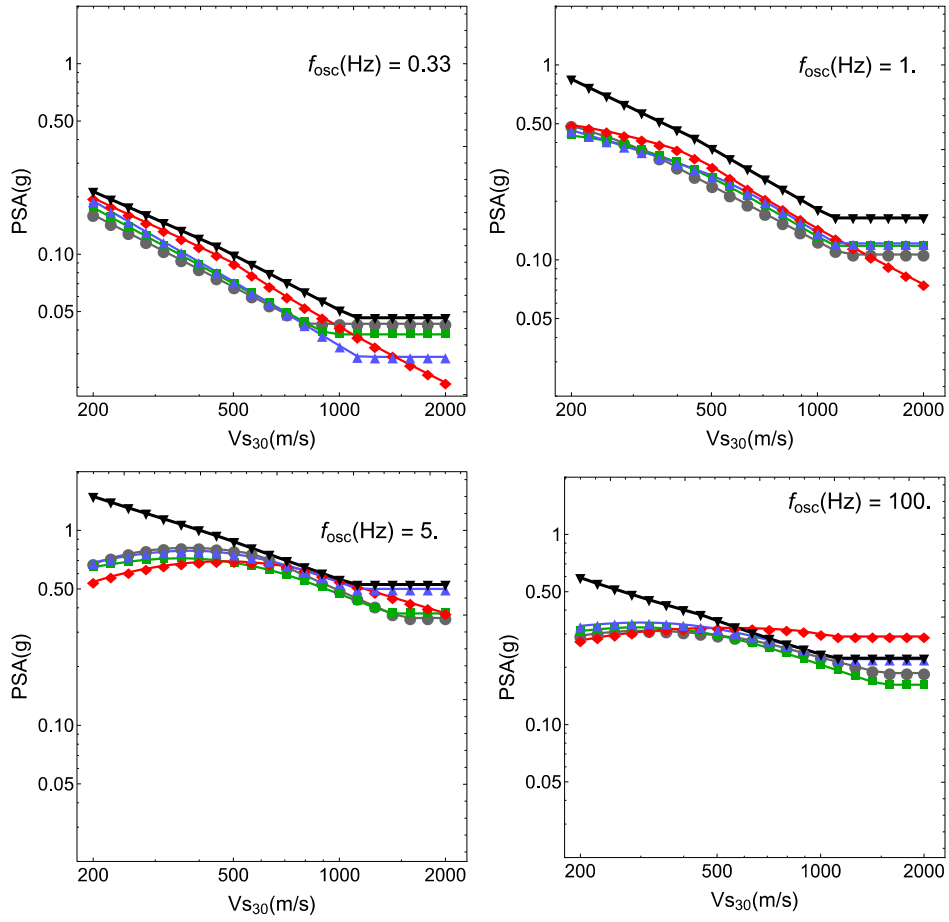

Figure 18. Comparison of V_{S30} scaling of the median predictions for an **M**7 earthquake at distance $R_{JB} = 10$ km.

residuals were then decomposed into between- and within-event components using the random-effects regression technique (Bates et al. 2015), using the following equation:

$$\ln\left(\frac{PSA_{obs}}{PSA_{mod}}\right) = \eta_e + \eta_s + \varepsilon \tag{20}$$

In Equation 20, the definitions of η_e, η_s, and ε remain the same as in Equation 1. The plots of response spectral residuals are shown in Figures A2, A3, and A4 provided in the online Appendix. Although the PSA residuals are not computed directly as the outcome of a standard regression procedure, overall, a stable variation of residuals around zero indicates the robustness of the model predictions obtained from our approach. In Figure A2, the between-event residuals are plotted for $f_{osc} = 0.5$, 3.33, 5, and 100 Hz (PGA). The between-events residuals are segregated according to regions, CA, IT, TW, and OTH, to investigate regional

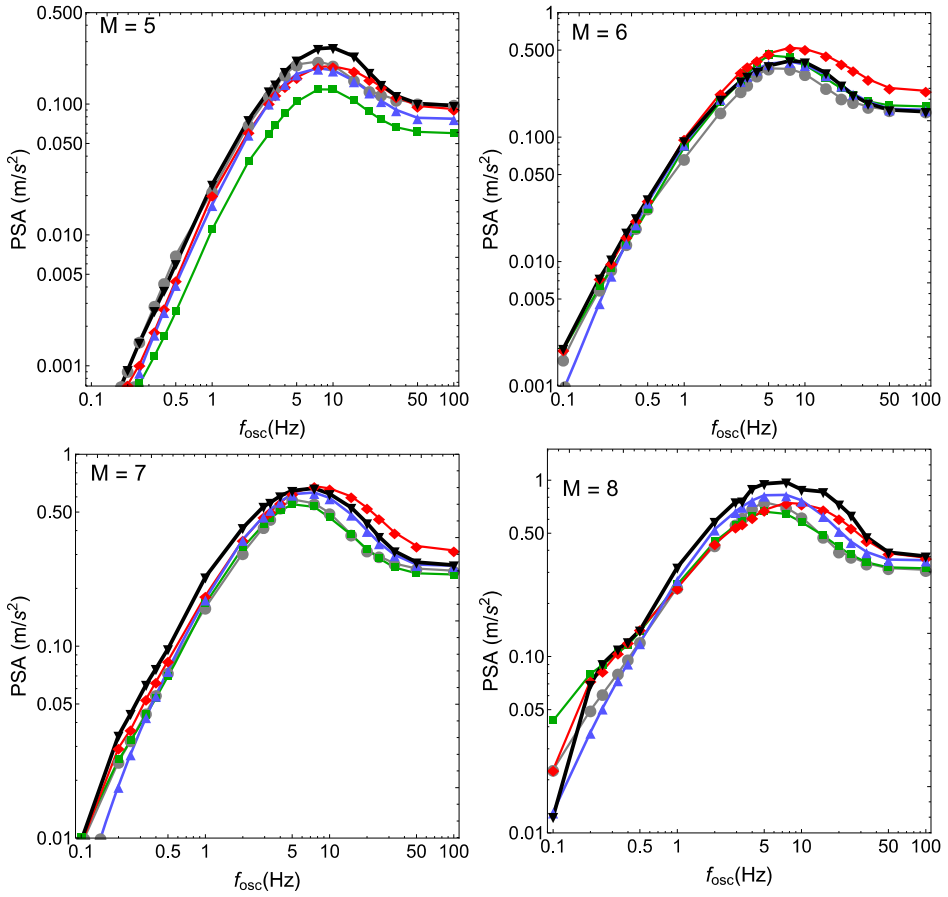

Figure 19. Comparison of median response spectra at a distance $R_{JB} = 10\,\text{km}$ for $V_{S30} = 800\,\text{m/s}$.

biases. However, no clear regional trend was observed. In Figure A3, the between-station residuals are plotted for the different regions separately at $f_{osc} = 0.5$, 5, and 100 Hz (PGA). In Figure S4, the single-station within-event residuals are plotted for $f_{osc} = 0.5$, 5, and 100 Hz (PGA). To investigate the relative regional variations in anelastic attenuation, the within-event residuals are plotted separately for CA, Japan, IT, and TW. Although there are not enough recordings from other regions, relatively high anelastic attenuation for Japan and IT can be observed, as also found by BSSA14. It is interesting to note that the FAS (within-event) residuals did not indicate any regional bias.

The standard deviations of the residual components were found to depend upon predictor variables (heteroscedasticity), as observed in NGA-West2 models (ASK14, BSSA14, CB14, and CY14). Thus, we recommend our variability components, depending upon different magnitude, distance, and V_{S30} ranges. We present τ in three magnitude ranges: (1) $\mathbf{M} \leq 4.5$, (2) $4.5 < \mathbf{M} \leq 6$, and (3) $\mathbf{M} > 6$. For this purpose we segregated η_e into

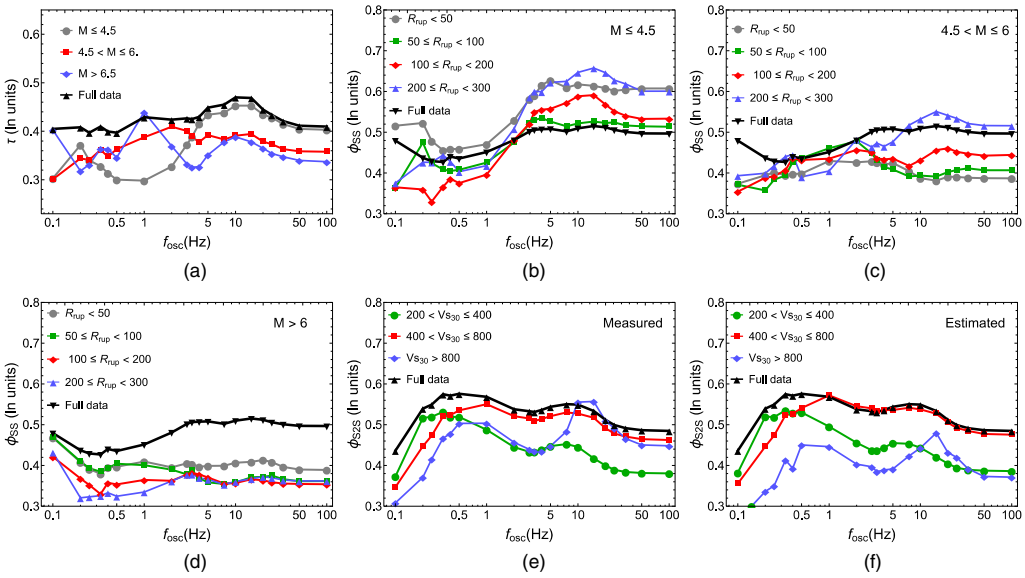

Figure 20. Plots of variability components: (a) Between-event residual standard deviation (τ), (b) single-station within-event residual standard deviation (ϕ_{SS}) for $\mathbf{M} \leq 4.5$, (c) ϕ_{SS} for $4.5 < \mathbf{M} \leq 6$, (d) ϕ_{SS} for $\mathbf{M} > 6$, (e) between-station residual standard deviation (ϕ_{S2S}) for sites with measured V_{S30}, and (f) ϕ_{S2S} for sites with estimated V_{S30}.

these three magnitude bins and computed τ in each bin at each oscillator frequency. Similarly, ϕ_{S2S} values are presented in three V_{S30} ranges: (1) $200 < V_{S30} \leq 400$ m/s, (2) $400 < V_{S30} \leq 800$ m/s, and (3) $V_{S30} > 800$ m/s. The ϕ_{SS} values are presented in three magnitude ranges ($\mathbf{M} \leq 4.5$,$4.5 < \mathbf{M} \leq 6$, and $\mathbf{M} > 6$), and in each magnitude bin, four distance ranges: $R_{rup} \leq 50$ km, $50 < R_{rup} \leq 100$ km, $100 < R_{rup} \leq 200$ km, and $R_{rup} > 200$ km. Figure 20 depicts the variability components in different predictor variable ranges. The variation of τ in different magnitude ranges over the entire oscillator frequency range is shown in Figure 20a. Figure 20b–20d shows the variation of ϕ_{SS} in the three magnitude and four distance ranges. Similarly, Figure 20e and 20f shows the variation of ϕ_{S2S} in the three V_{S30} ranges for the sites prescribed with the measured and estimated V_{S30} values, respectively. In Figure 20a, we clearly observe that τ is significantly higher for events $\mathbf{M} \leq 4.5$, in comparison to $\mathbf{M} > 4.5$, towards high oscillator frequencies. Likewise, the ϕ_{SS} for smaller events is larger at high-oscillator frequencies. Also, the ϕ_{SS} is smaller for near distances $R_{rup} \leq 100$ km and for $\mathbf{M} > 4.5$. The ϕ_{S2S} values are considerably lower for $200 < V_{S30} \leq 400$ m/s. The ϕ_{S2S} values for the station sites with measured V_{S30} values can be seen to be lower than those for the station sites with estimated V_{S30} values (Figure 20e and 20f). The τ, ϕ_{S2S}, and ϕ_{SS} values are presented in Tables A1, A2, and A3, respectively, provided in the online Appendix. From an application perspective, the total aleatory variability (σ) can be computed using the following equation:

$$\sigma = \sqrt{\tau^2 + \phi_{SS}^2 + \phi_{S2S}} \tag{21}$$

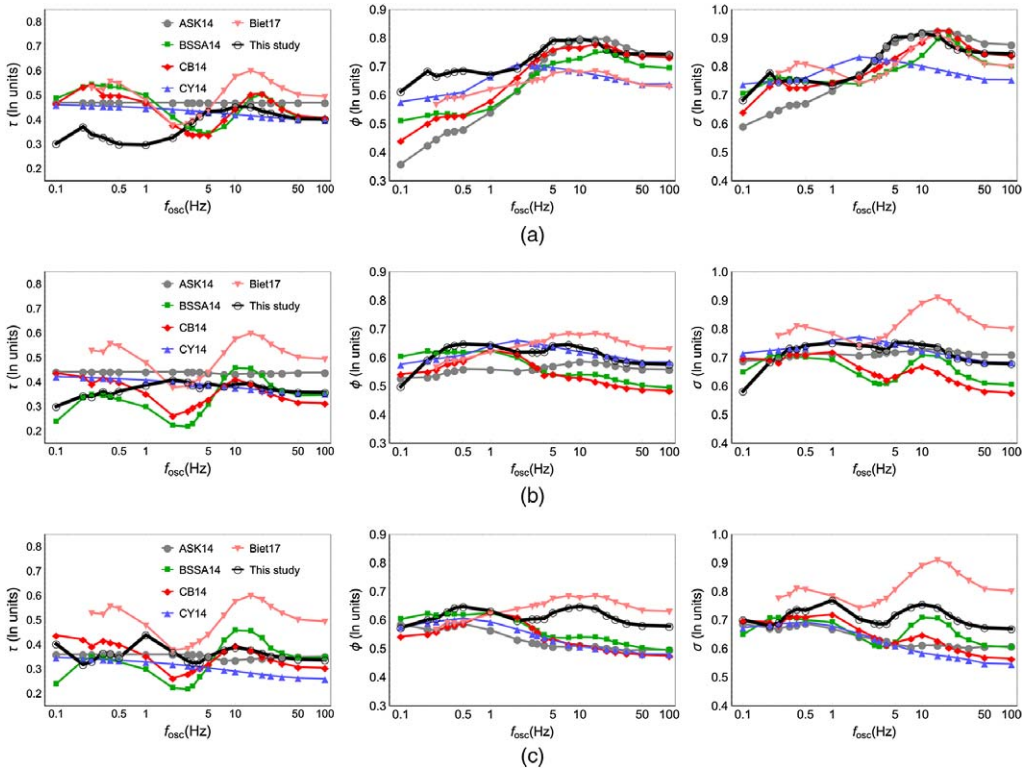

Figure 21. Comparison of standard deviations for (a) $\mathbf{M} \leq 4.5$, (b) $4.5 < \mathbf{M} \leq 6$, and (c) $\mathbf{M} > 6$. For NGA-West2 models the standard deviation values are obtained at $R_{rup} = 30$ km for $V_{S30} = 500$ m/s with other parameters having default values.

The values of τ, ϕ_{S2S}, and ϕ_{SS} should be selected from the corresponding tables depending upon the magnitude, distance, and V_{S30} scenario.

We compare the aleatory variability obtained from our approach with that from the NGA-West2 models considered for the comparisons in this article. Figure 21 depicts a comparison of the oscillator frequency dependence of the aleatory variability. In addition to the four NGA-West2 models (ASK14, BSSA14, CB14, and CY14), the model from Bindi et al. (2017) is also chosen for comparing variability in Figure 21. Comparisons amongst the six models are performed for between-event (τ), within-event ($\phi = \sqrt{\phi_{SS}^2 + \phi_{S2S}^2}$), and total ($\sigma$) standard deviations separately. The variabilities are shown for $R_{rup} = 30$ km and $V_{S30} = 500$ m/s in three magnitude ranges: (1) $\mathbf{M} \leq 4.5$, (2) $4.5 < \mathbf{M} \leq 6$ and (3) $\mathbf{M} > 6$. For the NGA-West2 models, the aleatory variability is shown for vertical strike-slip events with default parameter values. For the comparison in Figure 21, the variability values from the NGA-West2 models are computed for $\mathbf{M} = 4$, $\mathbf{M} = 5$, and $\mathbf{M} = 7$, corresponding to the three magnitude ranges, respectively.

In general, the total variability (σ) from our analysis is seen to be in reasonably good agreement with the other NGA-Wes2 models (ASK14, BSSA14, CB14, and CY14), except

for events in which $\mathbf{M} > 6$. However, in this magnitude range, our σ values are significantly lower than those of Bindi et al. (2017). The Bindi et al. (2017) values are seen in good comparison only for smaller events ($\mathbf{M} \leq 4.5$). The between-event standard deviation τ from our approach is in excellent comparison with other models in all three magnitude ranges. The within-event standard deviations ϕ from our approach for $\mathbf{M} > 6$ is higher towards high oscillator frequencies. Note that we have used ϕ_{S2S} corresponding to the station sites with measured V_{S30} values for computing σ in Figure 21. The higher ϕ, mainly at high-oscillator frequencies, can be attributed to the fact that the ϕ_{S2S} is higher towards high oscillator frequencies for $V_{S30} > 400$ m/s, as can be noticed from Figure 20. This increase in ϕ_{S2S} for $V_{S30} > 400$ can be due to the fewer number of sites in this V_{S30} range. Because of the higher ϕ, the total standard deviation (σ) from our approach is slightly higher than that from ASK14, CB14, and CY14 while rather comparable to that from BSSA14. Note that the NGA-West2 models provide models for the aleatory variability, while we present the actual variability values. The variability (σ) from our approach also contains an additional component-to-component variability (σ_c) as we use individual component records (both the components) for our analysis, while the NGA-West2 models use an average component. It is worth mentioning that the σ_c computed using the Boore (2005) ranges between 0.14–0.3 in natural log-units for the selected dataset.

RANGE OF APPLICABILITY

The functional forms of our FAS and D_{rvto} models are rather simple. They require magnitude, distance, and V_{S30} as predictor variables. The models are applicable for distances in the range 0–300 km and magnitudes 3–8, keeping in mind that the largest magnitude in the NGA-West2 dataset is $\mathbf{M}$ 7.9. With regard to V_{S30} values, it is applicable in the range 200–1,000 m/s, as the model is not well constrained at $V_{S30} > 1{,}000$ m/s. Also, we would like to make it clear that the duration (D_{rvto}) obtained in this study is valid for 5% critical damping, i.e., $\zeta = 0.05$.

It is beyond the scope of this article to demonstrate a complete procedure for how the method will be used to generate ground motions in regions with inadequate data. However, to provide some guidance in this regard, we discuss a few important points here. To adjust the FAS model, one can derive the seismological parameters, such as the stress parameter, anelastic attenuation, and site-attenuation parameter (κ), directly from the same (host) dataset (as performed in Bora et al. 2015) and try to adjust them in the empirical model using the target parameter values determined independently from the recordings of available (often smaller-magnitude) events. Thus, the entire adjustment is performed in the Fourier domain, consistent with the linearity property of a Fourier transform. An alternate procedure to get the host model consistent seismological parameters is to directly invert the Fourier spectrum obtained from the present empirical model, e.g., the between-station residuals of an FAS model can be used to obtain an indirect estimate of the site-amplification factor and parameter κ. Though it is not yet investigated, we believe that the ratio of ground motion duration from host-to-target region can be used to adjust the durations. The adjusted FAS and duration should be used within RVT framework to obtain the adjusted PSA values.

CONCLUSIONS

As mentioned in the *Introduction* section of this article, the recent findings of Stafford et al. (2017) have shown that the response spectral site-amplification factors exhibit scenario dependence for smaller-magnitude earthquakes. This has important consequences for performing seismic hazard analysis, mainly in low-to-moderate seismicity areas where recordings only from smaller events are available. Stafford et al. (2017) have also noted that empirical Fourier models complemented with duration models (Bora et al. 2015) can be used to avoid such issues instead of using the traditional PSA-based GMPEs. Thus, this article presents an alternative model framework for predicting response spectral values in shallow active crustal regions calibrated on the recently compiled NGA-West2 database. The approach consists of developing two separate models for FAS and a unique measure of duration (D_{rvto}) of ground motion. The two models are subsequently combined within the RVT framework to obtain the response spectral values. Our measure of duration (D_{rvto}) for an acceleration trace is computed in a such way that the RVT-based PSA (using the actual FAS) matches the actual PSA of that trace. Boore and Thompson (2015) have also suggested a duration measure for use in RVT that is based upon the time interval between 20–80% levels of Arias intensity.

Our empirical models for FAS and D_{rvto} are simple, and they include a fewer number of predictor variables as compared to the NGA-West2 models (Bindi et al. 2017). While most of the findings of our FAS model were confirmed by NGA-West2 models, our oscillator frequency–dependent duration model indicates that the dependence of duration on V_{S30} is rather weak. Also, we observe a weak dependence of duration over magnitude, mainly for $\mathbf{M} \leq 5.3$. We found that the between-event variability of the D_{rvto} model is much smaller in comparison to that of the FAS model. Mainly for Japan, the FAS residuals indicate a clear dependence over the basin depth parameter $Z_{1.0}$, i.e., increasing amplification with increasing $Z_{1.0}$. The dependence of between-event residuals for FAS on Z_{tor} was not clear, while it was rather clear for D_{rvto} (between-event) residuals at low oscillator frequencies, indicating shorter durations for deeper events. A comparison of D_{rvto} between-station residuals with $Z_{1.0}$ indicates that the station sites in Japan with deeper soil deposits exhibit relatively longer D_{rvto}. Also, we did not observe any regional bias in residuals analysis of the FAS and duration models. However, we observed a regional bias in response spectra (within-event residuals), indicating regionally varying anelastic attenuation (BSSA14).

The median response spectral predictions from our approach were found to be in excellent comparison with other NGA-West2 models, which allows our approach to be used as a standalone model for predicting response spectra. The within-event response spectral residuals indicate that the data from Japan and IT belong to an anelastic attenuation regime that is higher than the average (e.g., CA). The aleatory variability of PSA values from our analysis depends upon magnitude, distance, and V_{S30}. The σ from this study is found to be comparable to the NGA-West2 models (ASK14, BSSA14, CB14, and CY14) for a small to moderate magnitude range ($\mathbf{M} \leq 6$). For larger magnitudes, the σ values from this study are slightly higher than the NGA-West2 models. However, this comparison of variability should be seen in this light, that we include (often used) fewer numbers of variables in our models, along with simple functional forms. Bindi et al. (2017) have also obtained higher variability values for their model by using a simple functional form and fewer numbers of predictor variables.

Also, we do not use an average component (average of the two horizontal components) for deriving our models.

The present models are a significant improvement over Bora et al. (2015; derived over the European database), as they provide a reliable description of recorded ground motion over a wide range of magnitudes, distances, and site conditions. It is the first time that our approach of deriving response spectral amplitudes (Bora et al. 2014, 2015) is calibrated on the NGA-West2 database. To the best of our knowledge, it is also the first time that an empirical FAS model, such as in this study, is derived for any of the NGA databases. Additionally, we present an empirical model for the oscillator frequency–dependent duration, which is measured in a way to predict the PSA values using RVT along with an empirically derived FAS model.

ACKNOWLEDGMENTS

The French Electric Company (EDF) funded this work (Sigma Project), and we thank Paola Traversa for her scientific suggestions and support. Donat Fäh is thanked for his support and discussion in revising the manuscript. We thank D. Boore and two anonymous reviewers for their constructive comments and feedback. Dino Bindi and Sreeram Reddy Kotha are thanked for their initial support with the *lme4* R package. The metadata flat files and time-history records were downloaded from the NGA-West2 Pacific Earthquake Engineering Research Center (PEER) database (http://ngawest2.berkeley.edu/). All the plots were generated in Mathematica software. The mixed-effects regression R package *lme4* was used for regression.

APPENDIX

Please refer to the online version of this manuscript to access the supplementary material provided in the Appendix.

REFERENCES

Abrahamson, N. A., Silva, W. J., and Kamai, R., 2014. Summary of the ASK14 ground motion relation for active crustal regions, *Earthquake Spectra* **30**(3), 1025–1055.

Afshari, K., and Stewart, J. P., 2016. Physically parameterized prediction equations for significant duration in active crustal regions, *Earthquake Spectra* **32**(4), 2057–2081.

Akkar, S., Sandıkkaya, M. A., Şenyurt, M., Sisi, A. A., Ay, B. Ö., Traversa, P., Douglas, J., Cotton, F., Luzi, L., Hernandez, B., and Godey, S., 2014. Reference database for seismic ground-motion in Europe (RESORCE), *Bulletin of Earthquake Engineering* **12**(1), 311–339.

Al Atik, L., Abrahamson, N., Bommer, J. J., Scherbaum, F., Cotton, F., and Kuehn, N., 2010. The variability of ground-motion prediction models and its components, *Seismological Research Letters* **81**(5), 794–801.

Ancheta, T. D., Darragh, R. B., Stewart, J. P., Seyhan, E., Silva, W. J., Chiou, B. S. -J., Wooddell, K. E., Graves, R. W., Kottke, A. R., Boore, D. M., Kishida, T., and Donahue, J. L., 2014. NGA-West2 database, *Earthquake Spectra* **30**(3), 989–1005.

Atkinson, G. M., 2008. Ground-motion prediction equations for eastern North America from a referenced empirical approach: Implications for epistemic uncertainty, *Bulletin of the Seismological Society of America* **98**(3), 1304–1318.

Atkinson, G. M., and Boore, D. M., 1995. Ground-motion relations for eastern North America, *Bulletin of the Seismological Society of America* **85**(1), 17–30.

Atkinson, G. M., and Boore, D. M., 2006. Earthquake ground-motion prediction equations for eastern North America, *Bulletin of the Seismological Society of America* **96**(6), 2181–2205.

Atkinson, G. M., and Silva, W., 2000. Stochastic modeling of California ground motions, *Bulletin of the Seismological Society of America* **90**(2), 255–274.

Bates, D., Mächler, M., Bolker, B. M., and Walker, S. C., 2015. Fitting linear mixed-effects models using lme4, *Journal of Statistical Software* **67**(1), 1–48.

Bindi, D., Cotton, F., Kotha, S. R., Bosse, C., Stromeyer, D., and Grünthal, G., 2017. Application-driven ground motion prediction equation for seismic hazard assessments in non-cratonic moderate-seismicity areas, *Journal of Seismology* **21**(5), 1201–1218.

Bommer, J. J., and Martínez-Pereira, A., 1999. The effective duration of earthquake strong motion, *Journal of Earthquake Engineering* **3**(2), 127–172.

Bommer, J. J., Stafford, P. J., and Alarcón, J. E., 2009. Empirical equations for the prediction of the significant, bracketed, and uniform duration of earthquake ground motion, *Bulletin of the Seismological Society of America* **99**(6), 3217–3233.

Boore, D. M., 2003. Simulation of ground motion using the stochastic method, *Pure and Applied Geophysics* **160**(3–4), 635–676.

Boore, D. M., 2005. ERRATUM: Equations for estimating horizontal response spectra and peak acceleration from Western North American earthquakes: A summary of recent work, *Seismological Research Letters* **76**(3), 368–369.

Boore, D. M., Stewart, J. P., Seyhan, E., and Atkinson, G. M., 2014. NGA-West2 equations for predicting PGA, PGV, and 5% damped PSA for shallow crustal earthquakes, *Earthquake Spectra* **30**(3), 1057–1085.

Boore, D. M., and Thompson, E. M., 2015. Revisions to some parameters used in stochastic-method simulations of ground motion, *Bulletin of the Seismological Society of America* **105**(2A), 1029–1041.

Bora, S. S., Scherbaum, F., Kuehn, N., and Stafford, P., 2014. Fourier spectral- and duration models for the generation of response spectra adjustable to different source-, propagation-, and site conditions, *Bulletin of Earthquake Engineering* **12**(1), 467–493.

Bora, S. S., Scherbaum, F., Kuehn, N., and Stafford, P., 2016. On the relationship between Fourier and response spectra: Implications for the adjustment of empirical ground-motion prediction equations (GMPEs), *Bulletin of the Seismological Society of America* **106**(3), 1235–1253.

Bora, S. S., Scherbaum, F., Kuehn, N., Stafford, P., and Edwards, B., 2015. Development of a response spectral ground-motion prediction equation (GMPE) for seismic-hazard analysis from empirical Fourier spectral and duration models, *Bulletin of the Seismological Society of America* **105**(4), 2192–2218.

Brune, J. N., 1970. Tectonic stress and the spectra of seismic shear waves from earthquakes, *Journal of Geophysical Research* **75**(26), 4997–5009.

Brune, J. N., 1971. Correction, *Journal of Geophysical Research* **76**(20), 5002.

Campbell, K. W., 2003. Prediction of strong ground motion using the hybrid empirical method and its use in the development of ground-motion (attenuation) relations in eastern North America, *Bulletin of the Seismological Society of America* **93**(3), 1012–1033.

Campbell, K. W., and Bozorgnia, Y., 2014. NGA-West2 ground motion model for the average horizontal components of PGA, PGV, and 5% damped linear acceleration response spectra, *Earthquake Spectra* **30**(3), 1087–1115.

Chiou, B. S. -J., and Youngs, R. R., 2014. Update of the Chiou and Youngs NGA model for the average horizontal component of peak ground motion and response spectra, *Earthquake Spectra* **30**(3), 1117–1153.

Gregor, N., Abrahamson, N. A., Atkinson, G. M., Boore, D. M., Bozorgnia, Y., Campbell, K. W., Chiou, B. S. -J., Idriss, I. M., Kamai, R., Seyhan, E., Silva, W., Stewart, J. P., and Youngs, R., 2014. Comparison of NGA-West2 GMPEs, *Earthquake Spectra* **30**(3), 1179–1197.

Kempton, J. J., and Stewart, J. P., 2006. Prediction equations for significant duration of earthquake ground motions considering site and near-source effects, *Earthquake Spectra* **22**(4), 985–1013.

Konno, K., and Ohmachi, T., 1998. Ground-motion characteristics estimated from spectral ratio between horizontal and vertical components of microtremor, *Bulletin of the Seismological Society of America* **88**(1), 228–241.

Lee, J., and Green, R. A., 2014. An empirical significant duration relationship for stable continental regions, *Bulletin of Earthquake Engineering* **12**(1), 217–235.

Montejo, L. A., and Vidot-Vega, A. L., 2017. An empirical relationship between Fourier and response spectra using spectrum-compatible times series, *Earthquake Spectra* **33**(1), 179–199.

Raghu Kanth, S. T G., and Iyenger, R. N., 2007. Estimation of seismic spectral acceleration in peninsular India, *Journal of Earth System Science* **116**(3), 199–214.

Rietbrock, A., Strasser, F., and Edwards, B., 2013. A stochastic earthquake ground-motion prediction model for the United Kingdom, *Bulletin of the Seismological Society of America* **103**(1), 57–77.

Sandıkkaya, M. A., and Akkar, S., 2017. Cumulative absolute velocity, Arias intensity and significant duration predictive models from a pan-European strong-motion dataset, *Bulletin of Earthquake Engineering* **15**(5), 1881–1898.

Seyhan, E., and Stewart, J. P., 2014. Semi-empirical nonlinear site amplification from NGA-West2 data and simulations, *Earthquake Spectra* **30**(3), 1241–1256.

Stafford, P. J., Rodriguez-Marek, A., Edwards, B., Kruiver, P. P., and Bommer, J. J., 2017. Scenario dependence of linear site effect factors for short-period response spectral ordinates, *Bulletin of the Seismological Society of America* **107**(6), 2859–2872.

Toro, G. R., Abrahamson, N. A., and Schneider, J. F., 1997. Model of strong ground motions from earthquakes in eastern and central North America: Best estimates and uncertainties, *Seismological Research Letters* **68**(1), 41–57.

Yenier, E., and Atkinson, G. M., 2015. Regionally adjustable generic ground-motion prediction equation based on equivalent point-source simulations: Application to central and eastern North America, *Bulletin of the Seismological Society of America* **105**(4), 1989–2009.

(Received 3 November 2017; Accepted 23 July 2018)